Bioorganic Chemistry 82 (2019) 340–359

Contents lists available at ScienceDirect

Bioorganic Chemistry

journal homepage: www.elsevier.com/locate/bioorg

Design, synthesis, biological evaluation and dynamics simulation of indazole derivatives with antiangiogenic and antiproliferative anticancer activity

Nevine M.Y. Elsayed[a], Rabah A.T. Serya[a], Mai F. Tolba[b], Marawan Ahmed[c], Khaled Barakat[c,d,e], Dalal A. Abou El Ella[a,f], Khaled A.M. Abouzid[a,g,*]

[a] Pharmaceutical Chemistry Department, Faculty of Pharmacy, Ain Shams University, Abbassia, Cairo 11566, Egypt
[b] Pharmacology and Toxicology Department, Faculty of Pharmacy, Ain Shams University, Abbassia, Cairo 11566, Egypt
[c] Faculty of Pharmacy and Pharmaceutical Sciences, University of Alberta, Edmonton, Alberta, Canada
[d] Li KaShing Institute of Virology, University of Alberta, Edmonton, Alberta, Canada
[e] Li KaShing Applied Virology Institute, University of Alberta, Edmonton, Alberta, Canada
[f] Department of Pharmaceutical Chemistry, Faculty of Pharmacy, Nahda University, Beni Suef, Egypt
[g] Department of Organic and Medicinal Chemistry, Faculty of Pharmacy, University of Sadat City, Menoufia, Egypt

ARTICLE INFO

Keywords:
Indazole
Dynamics
VEGFR-2
Anticancer

ABSTRACT

VEGFR-2 has a pivotal role in promoting cancer angiogenesis. Herein, two series of novel indazole-based derivatives were designed, synthesized and evaluated for their *in vitro* inhibitory action against VEGFR-2 kinase enzyme. The second series **11a-e** exhibited better potency than the first one **7a-d** and **8a-f**. Compounds **11b**, **11c** and **11e** exhibited the most potent action, with IC_{50} of 5.4 nM, 5.6 nM and 7 nM, respectively. As a measure of cellular VEGFR-2 inhibition, compounds **11b** and **11c** showed strong inhibition of human umbilical vein endothelial cells (HUVEC) proliferation with 80% and 99.6% inhibition at 10 μM concentration, respectively. Attempting to interpret SAR of the synthesized compounds, and provide a basis for further optimization; a comprehensive modeling study was implemented. Molecular docking, dynamics simulation and free energy calculation of the synthesized compounds along with known VEGFR-2 inhibitors were applied. The study illustrated the effect of several factors on VEGFR-2 inhibition, such as the interaction with solvent accessible region of the enzyme, the presence of NH linker and the degree of conformational restriction. Finally, our compounds were evaluated for their *in vitro* anti-proliferative effect against the full NCI panel of cancer cell lines, where compounds **11a** and **11c** displayed mean GI% of 93 and 130%, respectively, and showed partly a better behavior than the FDA approved drug sorafenib, with respect to activity (GI_{50}) and safety (LC_{50}) against several cell lines. Thus, compound **11c** represents a promising candidate for cancer treatment through antiangiogenic dependent and antiangiogenic independent modes of action.

1. Introduction

Antiangiogenic anticancer therapy was first introduced as a rational approach for cancer treatment, when Folkman and colleagues illustrated the urgency of neovascularization for tumors to grow beyond a limited volume (1–2 mm^3) [1–5]. Vascular endothelial growth factor (VEGF) family are the chief proangiogenic factors, which are secreted by the cancerous cells, where VEGF-A is the major mediator of angiogenesis [6–8]. VEGF family members target three correlated receptors (VEGFR 1–3), activating several signaling pathways. VEGFR-2 is the principal receptor of VEGF-A; it is responsible for vascular endothelial cell development, proliferation, invasion and migration [7,9]. Antiangiogenic agents targeting VEGF/VEGFR-2 signaling pathway include monoclonal antibodies against VEGF, as Bevacizumab [10], and small-molecule tyrosine kinase inhibitors [11] as Sorafenib [12], sunitinib [13], pazopanib [14], cabozantinib [15], lenvatinib [16], and apatinib [17].

Apart from the antiangiogenic effect of inhibiting VEGFR-2 signaling pathway, VEGFR-2 blockade can exert direct antiproliferative effect against cancer cell lines that express VEGFR-2 receptors on their surface. VEGFR-2 inhibitors induce apoptosis of these cell lines *in vitro*. They block the VEGFR-2 downstream signaling pathways, as PI3K/AKT, and Ras-MEK-ERK pathways [18,19]. VEGFR-2 receptors overexpression is characteristic of certain limited number of cell lines of various tumors, such as, colon [20], gall bladder [21], non-small cell lung [22,23], breast [24], prostate [25], and melanoma [26,27], human

* Corresponding author at: Pharmaceutical Chemistry Department, Faculty of Pharmacy, Ain Shams University, Abbassia, Cairo 11566, Egypt.
E-mail address: khaled.abouzid@pharma.asu.edu.eg (K.A.M. Abouzid).

https://doi.org/10.1016/j.bioorg.2018.10.071
Received 26 August 2018; Received in revised form 26 October 2018; Accepted 31 October 2018
Available online 02 November 2018
0045-2068/

hepatocellular carcinoma (HCC) [28], renal, ovarian and cervical [29] cancer and hematologic malignancies [18,30]. However, with respect to the complex nature of cancer disease, it is not surprising that anti-VEGFR-2 monotherapy–in several cases-exhibited little effect on cancer progression, due to the emerging resistance in some individuals or the resistant nature of some cancers [31].

The VEGFR-2 catalytic domain toggles between active and inactive states, through the movement of the DFG motif (Asp-Phe-Glu) of the activation lobe [32,33]. Movement of the DFG loop allows the phenyl ring of the phenylalanine amino acid to rotate around the C—N bond of aspartate, displacing itself for > 10 Å into the ATP binding pocket, voiding a back hydrophobic pocket. As the phenyl ring of phenylalanine partially occupies the space usually utilized by ATP for performing phosphorylation, the DFG-out conformation inhibits ATP binding and thus, renders the kinase in an inactive state [34]. Both conformations can be targeted by VEGFR-2 tyrosine kinase inhibitors (TKIs) [35]. VEGFR-2 TKIs can be classified into two main types, type I and type II inhibitors [36]. Type I inhibitors target the active DFG-in conformation and bind the ATP binding site of the kinase. In contrast, type II inhibitors bind to the inactive DFG-out conformation through interacting with the ATP binding site as well as the hydrophobic back pocket [37,38]. It is noteworthy that some VEGFR-2 TKIs were classified as type III inhibitors [39,40], where they exclusively occupy the back pocket of the DFG-out conformer, without extending to the ATP site [41].

Cautious inspection of several VEGFR-2 potent inhibitors reveals certain common key interaction features that can be summarized, as shown in Fig. 1:

(A) Hinge binder: It consists of a flat aromatic ring system with a hydrogen bond acceptor for interaction with hinge region. The hydrogen bond acceptor makes an essential hydrogen bond with NH of Cys919, while the aromatic ring is normally involved in π-π interaction with phenyl ring of Phe918 [42].
(B) Extra central aromatic ring system: It is located in the proper position to provide π-π interactions with Phe1047 (as in vandetanib or π-cation interaction with Lys 868 (as in pazopanib, axitinib and linifanib) [42,43].
(C) Features targeting the back hydrophobic pocket (in type II inhibitors only): They are responsible for bridging hydrogen-bond network between with CO of Glu885 and the NH of Asp1046 involved in the DFG loop move. In the same time, they bear an aromatic ring with hydrophobic substitution that extends to occupy the back hydrophobic pocket. Aryl urea and substituted benzamide are most commonly used to satisfy these requirements (as in sorafinib and linifanib) [34,42].

In this study, the main objective was to design novel potent indazole-based VEGFR-2 kinase inhibitors, applying conformational restriction strategy and explore the influence of rigidification on the biological activity of both type I and type II inhibitors, using various modeling techniques.

Conformational rigidification has been employed as a successful strategy in the drug design and development process [44,45]. The efficiency of conformational restriction is attributed to its ability to lower the entropic cost of binding of the conformationally restricted derivative to the target, as compared to the more flexible derivative. Additionally, rigid derivatives tend to be more selective and metabolically-resistant than flexible ones. These advantages have been supported by the comparison of rigid and flexible derivatives with respect to biological activity, selectivity and pharmacokinetics [46].

In a previous study, we reported the development of a series of pyrimidine based VEGFR-2 inhibitors [47]. Compound **A** was the most active compound in which conformational restriction approach was applied (IC_{50} = 148 nM).

Herein, two rigidification strategies were adopted, as shown in Fig. 2**.** The first strategy involved incorporation of the N1 of urea moiety in an indazole ring, to give the target compounds **7a-d** and **8a-f**. This strategy has been previously implemented to yield highly potent derivatives, where naphthalene, benzoxazine and indole rings have been used in rigidification [48–54]. The second strategy was based upon restricting the rotation of the central aromatic ring by incorporating it in an indazole ring that is attached to the hinge binder directly at N1 position of the indazole ring, to give target compounds and **11a-e**. Such approach was adopted before in the design of type I inhibitors, using indole [55]. Although it didn't yield highly active agent (IC_{50} > 300 nM), we believed – based on the aforementioned observation – that potent type II inhibitors may be produced if careful structural modulation was adopted. In order to fully assess the influence of each strategy on the activity of type I and type II inhibitors, rigidification was also implemented in the design of parent compounds (**6b** and **9**), that lack the aryl urea group that interact with the back hydrophobic pocket of VEGFR-2 kinase enzyme, and thus, they are unable to target the inactive conformation of VEGFR-2 kinase.

The indazole ring is as an attractive choice for the rigidifiaction purpose. It can also yield compounds with acceptable solubility, PK properties [56], synthetic feasibility and versatility [57]. Indazole was previously implemented to design inhibitors that follow our first strategy, however, it yielded compounds with mediocre activity (IC_{50} = 2.3 μM) [54]. Herein, we proved that structural optimization can give more potent indazole-based compounds.

Quinazoline was our selected hinge binder. Several quinazoline-based VEGFR-2 inhibitors have been reported in literature [44,58–67]. Quinazoline exhibits optimum binding to the hinge region of the kinases [68], as it is capable of forming two hydrogen bonds with the hinge amino acid Cys919 and it is anchored in the hinge region by Pi-Pi interaction with Phe918.

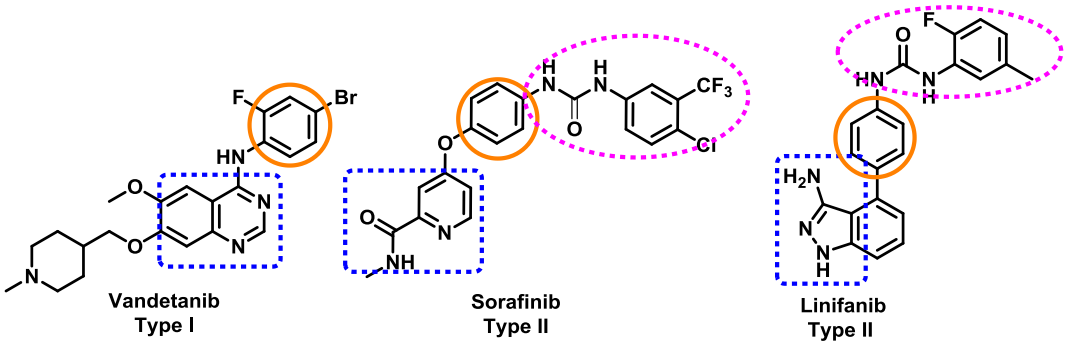

Fig. 1. Vandetanib, Sorafinib and Linifanib with their main pharmacophoric features. Hinge binders are indicated by blue dots, the central aromatic group is included in orange circle and the aryl urea derived group is indicated by pink dots.

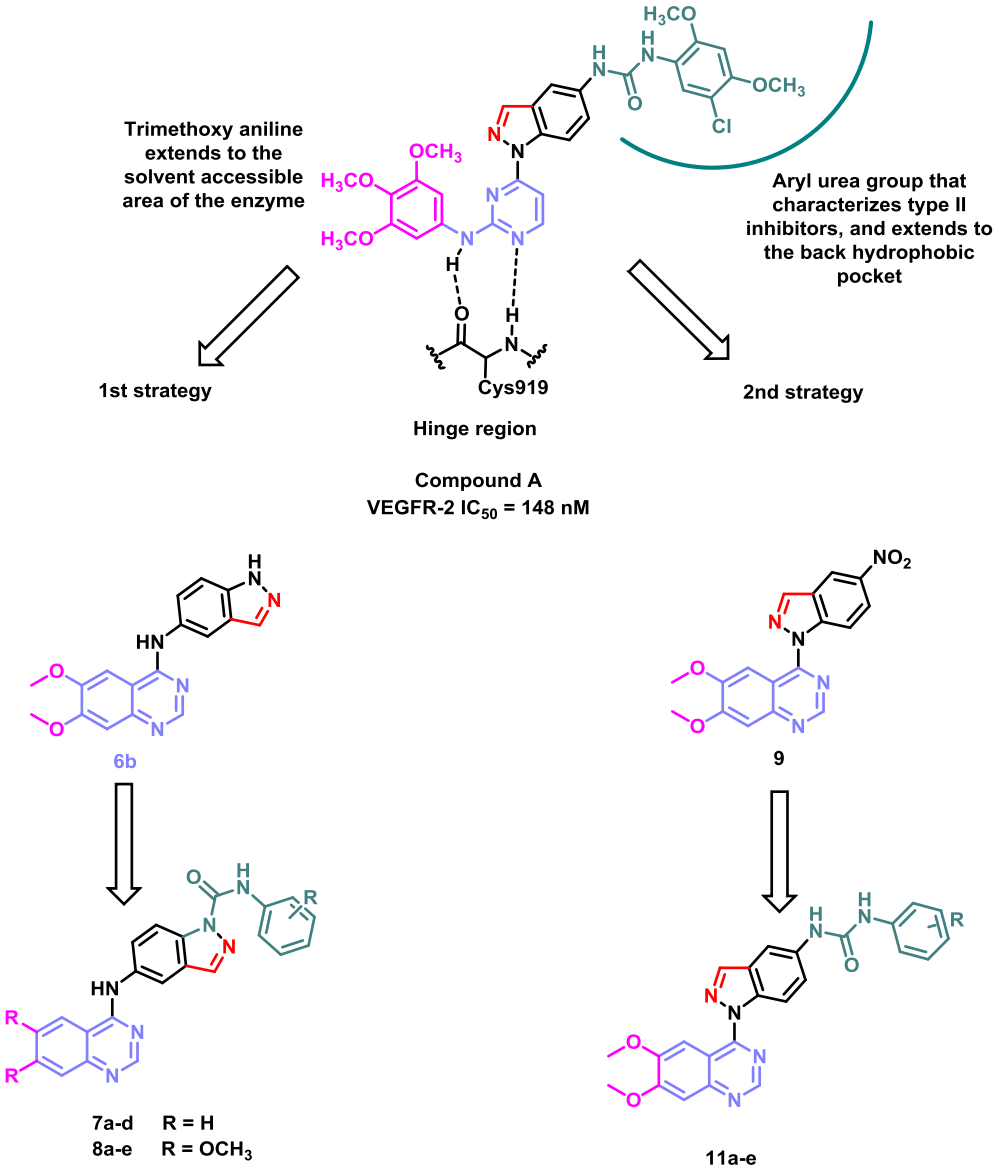

Fig. 2. The design strategies for the target compounds. Site of rigidification is marked with red color, hinge binder is colored in blue, aryl urea is colored in green, and solvent accessible region is colored in pink.

2. Results and discussion

2.1. Chemistry

The synthetic routes adopted for synthesis of the target compounds are outlined in Schemes 1–3. Diazotization of 2-methyl-4-nitroaniline **1** i yielded 5-nitroindazole **2** [69]. 5-aminoindazole 3 was obtained through the catalytic reduction of compound **2.** Nucleophilic substitution reaction between **3** and 2,4-dichloropyrimidine was employed to obtain compound **4**. Phenylisocyanate was added to compound **4** to give compound **5**.

As outlined in Scheme 2, Compounds **6a** and **6b** were constructed via the reaction between 5-aminoindazole **3** and the appropriate quinazoline derivative. Then, compounds **7a-d** and **8a-f** were synthesized using the same procedure mentioned under the synthesis of compound **5** by mixing equimolar amounts of **6a** or **6b** and the corresponding isocyanate.

As shown in Scheme 3, compound **2** was reacted with 6,7-dimeethoxy quinazoline in presence of NaH, to give compound **9**. The nitro group in compound **9** was reduced using H_2/Pd mixture to give compound **10** that was directly used in the following reaction. Compound **10** was reacted with the corresponding isocyanate to yield compounds **11a-e**.

2.2. Kinase inhibition assay

In Table 1, it is obvious that there is significant difference in activity between series **7a-d** and series **8a-f** even when they share the same substituents on the benzamide ring. This was attributed to the presence of dimethoxy substitution at positions 6 and 7 of the quinazoline ring that are supposed to extend to the solvent accessible region of the enzyme giving superior potency to series **8a-f** over series **7a-d**. Examination of the activity of compounds **8a-f** reveals pronounced variation depending on the substituent on the benzamide ring, where compound **8a**-with 3-chloro and 4-methyl substitution-was the most active compound while other compounds showed intermediate to strong activity. Also, the thio derivative **8f** showed comparable activity to **8a**, suggesting that S in **8f** maintains the H-bond with Asp1046 as O found in other compounds. There is a remarkable difference in activity between compound **5** and compound **8e**. This can indicate the

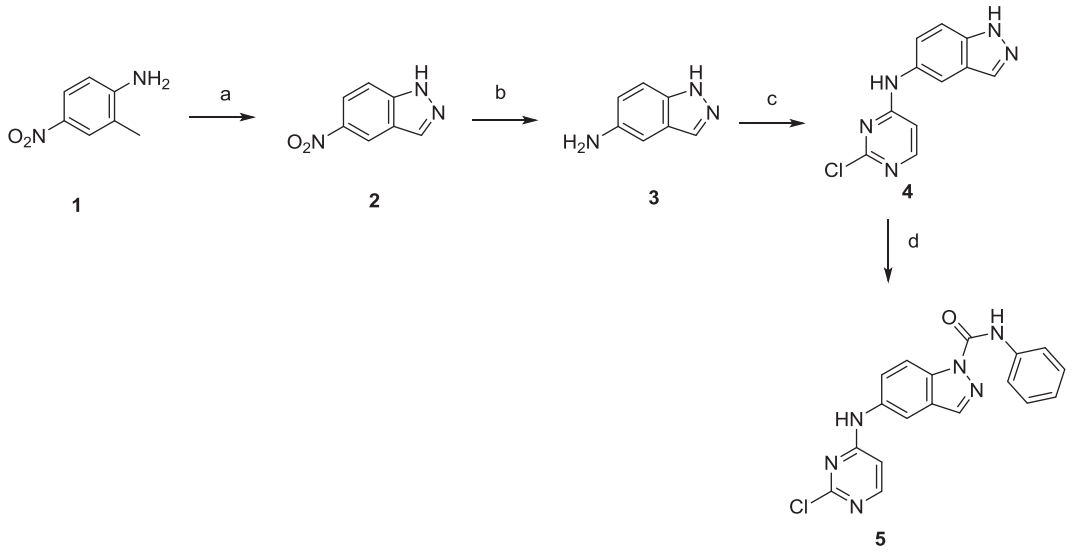

Scheme 1. *Reagents and conditions:* (a) $NaNO_2$, gl. AcOH, r.t., 72 h, 72%, (b) H_2, Pd/C, 10%, methanol, 40 °C, 30 psi, 3 h, 97.2%, (c) 2,4-dichloropyrimidine, TEA, ethanol, reflux, 5hrs, 78.59%, (d) phenylisocyanate, dry THF, r.t., 24 h, 66.4%.

inefficiency of 2-chloropyrimidine as hinge binder, when compared to 6,7-dimethoxyquinazoline. Unlike **8a-f**, the series **11a-e** displayed an excellent activity profile, where compounds **11b**, **c** and **e** had IC_{50} of 5.4, 5.6 and 7 nM, respectively, showing superior potency against VEGFR-2 than sorafenib (IC_{50} = 90 nM [12]), while **11a** exhibited a relatively low activity (IC_{50} = 83 nM), and **11d** exerted the weakest inhibitory action among the series (mean% inhibition = 86%). Thus, it can be concluded that increasing the bulkiness of the terminal phenyl ring by disubstitution (**11b** and **11c**) or trisubstitution (**11e**) is favorable for VEGFR-2 inhibitory activity. Nevertheless, using large bulky substituents (as in compound **11d**) may hinder the binding to the enzyme. Compounds **6b** and **9** lacked the aryl urea moiety, yet they displayed interesting activity profiles when compared with analogous compounds that carried the aryl urea group. While compound **6b** showed good activity (mean% inhibition = 100%), compound **9** showed compromised inhibitory action against the enzyme (mean% inhibition = 46%), when compared with series **11a-e**, supporting the claim that our second design strategy is not suitable for developing potent type I VEGFR-2 kinase inhibitors, while it is efficient in the design of type II VEGFR-2 inhibitors with good activity.

2.3. In vitro HUVEC Anti-proliferative assay

The most active compounds against VEGFR-2 kinase (**11b** and **c**) were preliminarily evaluated for HUVEC (human umbilical vein endothelial cells) proliferation inhibition assay at a concentration of 10 μM. (HUVECs) cell line is an ideal model system for studying the cellular antiangiogenic effect *in vitro*, as they are good representatives of the behavior of vascular endothelial cells *in vivo*. Besides, they are relatively easy to harvest from large blood vessels [70,71]. As shown in Table 2., **11b** and **11c** had 80% and 99.6% inhibition, respectively, indicating that they can exert cellular antiangiogenic effect based upon their action against VEGFR-2 kinase. Later, IC_{50} against HUVEC cell line was determined for the most active compound **11c**, where it showed IC_{50} of 87.7 nM, with sorafenib as a reference (IC_{50} = 160 nM).

2.4. In vitro anticancer activity

Compounds with pronounced inhibitory potency against VEGFR-2 (**8a**, **8f**, **11a**, **11b**, **11c**, and **11e**) were submitted to the National Cancer Institute (NCI) Developmental Therapeutic Program (www.dtp.nci.nih.gov). Four compounds **8a, 11a, 11b, and 11c** were selected to be screened for *in vitro* anticancer action. The selection was based on several factors, including: the novelty of the structure, drug-likeness, absence of problematic moieties (such as nitro, nitroso and flexible acyclic group) and the likeability of the compound to display an antineoplastic action, based on its structure [72]. The assays were executed according to the protocol of the Drug Evaluation Branch, NCI, Bethesda tested [73].

The compounds showed variable anticancer activity. Compounds **8a**

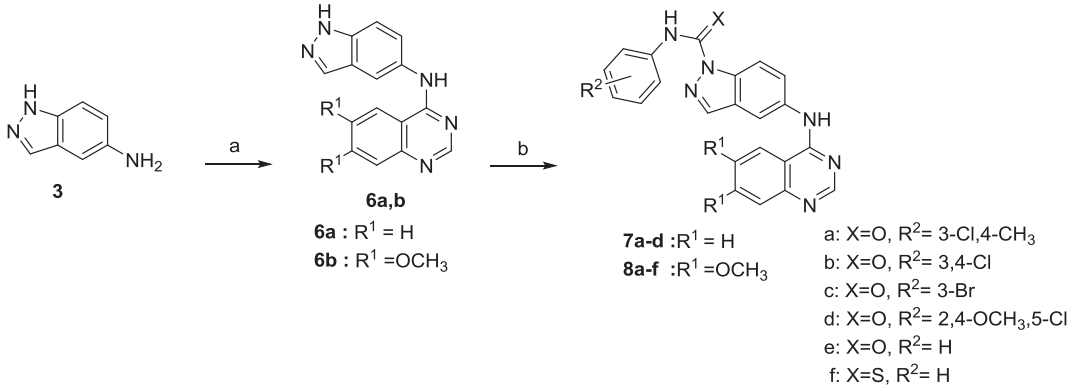

Scheme 2. *Reagents and conditions:* (a) isopropanol, reflux, 3hrs, 4-chloroquinazoline (for compound **6a**), 48.92% – 4-chloro-6,7-dimethoxyquinazoline (for compound **6b**), 81.54%, (b) isocyanates or isothiocyanate, THF or DMF, r,t., 24 h, 10.51–88%.

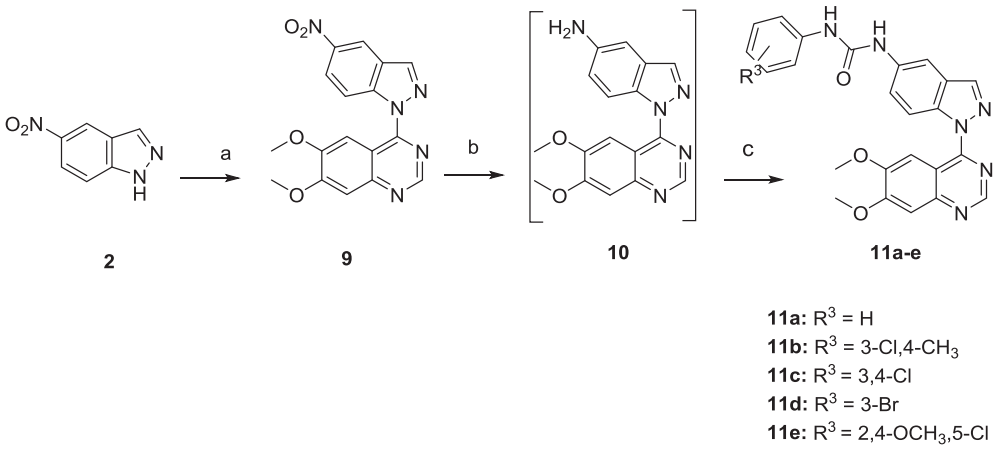

Scheme 3. *Reagents and conditions:* (a) 4-chloro 6,7-dimethoxyquinazoline, NaH, DMF, 0 °C, 6 h, 83.58%, (b) H_2, Pd/C 10%, 40 °C, 50 psi, THF, overnight. (c) Aryl isocyanate, DCM, r.t., 24 h, 34–44.5%.

and **11b** had fair anticancer activity, with their mean percentages growth inhibition (GI%) equal 13%, and 8%, respectively. However, **8a** exerted profound inhibitory action against (GI% > 50%) against NSCLC cell line NCI-H322M (60%), and breast cancer cell line MDA-MB-468 (90%). Similarly, **11b** had elicited selective anticancer activity against colon cancer cell line KM12 (74%), (see Supplementary file). In the light of these results, **11b**-which had potent action against VEGFR-2-showed a promising potential to be developed into a selective potent agent targeting colon cancer in personalized therapy. It is noteworthy that compounds **8a** and **11b** exhibited promising VEGFR-2 inhibition with IC_{50} values of 148 and 5.4 nM respectively, while showed poor antiproliferative activity, with mean percentages growth inhibition (GI %) of 13%, and 8%. This discrepancy in activity may indicate that both compounds exhibit their antitumor effect by selective action on endothelial cells rather than cancer cells via targeting targeting endothelial VEGFR-2 receptors leading to hampered angiogenesis and limiting blood supplies to the growing tumors [74]. Otherwise, this discrepancy may be attributed to the inability of these compounds to accumulate in the cancerous cells due to their physicochemical properties, thus they are unable to penetrate cell membrane, as observed in some previous cases [75,76].

Table 3 shows the results of screening of the most potent derivatives (**11a** and **11c**) for their growth inhibition against the panel of cell lines. On the others side, **11a** and **11c** showed high mean %GI (93 and 130% respectively). **11a** and **11c** exerted a profound antiproliferative effect against the full NCI panel of cell lines (%GI = or > 50%). Consequently, both compounds were evaluated against the NCI panel of tumor cell lines at five levels of concentration such that three parameters were calculated for each compound: GI50, TGI and LC50 – against each cell line, as presented in Tables 4. GI50 is the concentration that showed 50% growth inhibition, TGI (tumor growth inhibition) reflects cytostatic activity, while LC50 (50% lethal concentration) represents the cytotoxicity parameter for compounds.

Compounds **11a** and **11c** exerted significant potency against the full panel of cell lines. Compound **11a** showed a submicromolar activity against 23 cancer cell lines of different types where it exhibited its highest potency against T-47D breast cancer cell line (GI_{50} = 183 nM). Also, it had one digit micromolar GI_{50} on the rest of cell lines panel that ranged from 1.01 to 5.22 μM. Compound **11c** displayed nanomolar GI_{50} against two cell lines: KM12 colon cancer cell line (50 nM) and SF-539 CNS cancer cell line (612 nM). It had one digit micromolar GI_{50} on the rest of cell lines panel that ranged from 1.24 to 4.44 μM. Interestingly, **11c** elicited a good antiproliferative effect against the multi-drug resistant ovarian cancer cell line (NCI/ADR-RES) [77] with GI_{50} of 2.36 μM, maintaining excellent safety profile (LC_{50} > 100 μM).

Attempting to achieve a better evaluation for the *in vitro* anticancer activity of **11a** and **11c**, the results were compared to those of sorafenib (which were downloaded from https://dtp.cancer.gov/discovery_development/nci-60/). Sorafenib is a multi-kinase inhibitor [12], which is approved as a treatment for renal cell carcinoma, hepatocellular carcinoma, and thyroid cancer [31]. It is This comparison illustrated that **11a** had better antiproliferative potency than sorafenib through most of the NCI-60 panel, where **11a** displayed a lower GI_{50} than that of sorafenib against 52 cell lines of different types. Specifically, **11a** was more potent against renal cancer cell lines than sorafenib. With respect to safety, **11a** had higher LC_{50} than sorafenib at 23 cell lines, showing the most superior safety profile against CNS cell lines. In addition, it maintained better safety than sorafenib with respect to two of renal cell lines (SN12C and CAKI-1). In a similar way, **11c** exhibited greater potency than sorafenib against 39 cancer cell lines of all types (including all renal cell lines), maintaining better safety in 19 cell lines. **11c** had excellent safety profiles against leukemia and colon cancer cell lines. Based on the aforementioned facts, **11a** and **11c** had comparable *in vitro* anticancer activity to sorafenib, with a reasonable safety profiles, thus, they can be developed into clinical antitumor candidates.

Interpreting the *in vitro* anticancer behavior of **11a** and **11c** was not a straightforward process. In NCI panel of cell lines, several cell lines overexpress VEGFR-2, such as breast cell lines: T-47D, MCF7, and MDA-MB-231 [78,79], melanoma cell line: MDA-MB-435 [80], leukemia cell line: HL-60 [81], and colon cancer cell lines: HCT-116, HT29 [20]. The remaining cell lines exhibit variable levels of VEGFR-2 expression [67]. Generally, some tumors display high degree of sensitivity towards anti-VEGFR-2 therapy such as renal cell carcinoma, and ovarian tumors. On the contrary, other cell lines are known for their high resistance to VEGFR-2 inhibitory therapy, such as prostate cancer, and melanoma [31]. As a result, the inhibitory potency of the compounds against VEGFR-2 kinase can't interpret their superior wide spectrum *in vitro* anticancer activity, and further investigation was required. Compound **11c** showed several advantages as: the superior anti VEGFR-2 potency, the wide spectrum of *in vitro* anticancer activity (as illustrated by its high mean GI% of 130%), its antiproliferative activity against the resistant cell line NCI/ADR-RES of ovarian cancer, that exceeded that of sorafenib, and the acceptable level of safety – as demonstrated by the high LC_{50} values against several cell lines – compared to sorafenib. Of special interest, **11c** had superior safety to sorafenib with respect to leukemia and colon cell lines, suggesting that it can avoid two of the significant side effects of sorafenib, which are leukopenia and GIT distress [12,82]. Thus, it represents an excellent anticancer candidate for personalized therapy and resistant cancerous subtypes. Thus, it was chosen for further investigation of its angiogenic – independent mode of action. PC-3 prostate cancer cell line was chosen for the study, since it is

Table 1
In vitro VEGFR-2 inhibition data of synthesized compounds, showing mean % VEGFR-2 inhibition and IC_{50} values.*

Compound	R	VEGFR −2% Inhibition (10 μM)	IC_{50} (nM)
5	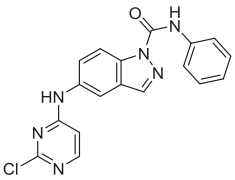	6	NT
6b	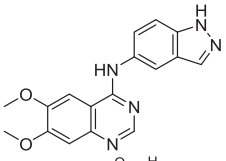	100	NT
7a	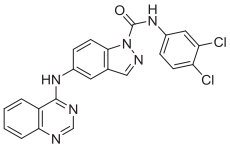	−4	NT
7b	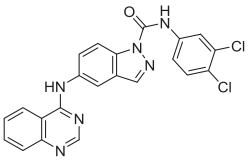	7	NT
7c	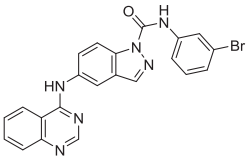	4	NT
7d	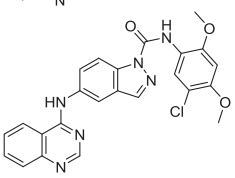	10	NT
8a	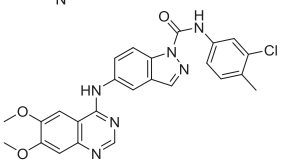	100	148
8b	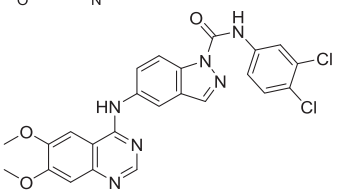	48	NT
8c	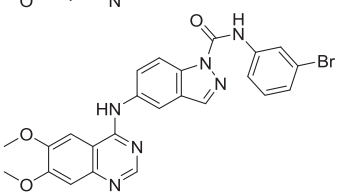	86	NT
8d	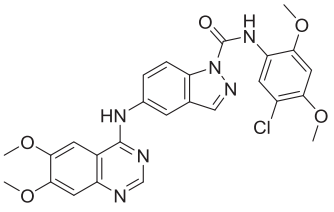	50	NT

(*continued on next page*)

Table 1 (*continued*)

Compound	R	VEGFR −2% Inhibition (10 μM)	IC_{50} (nM)
8e	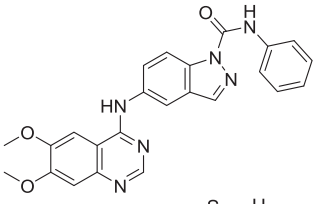	94	NT
8f	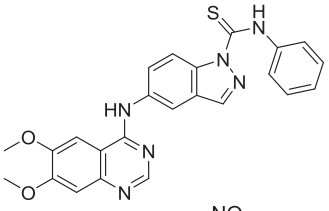	100	163
9	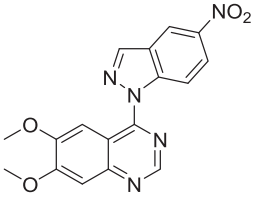	46	NT
11a	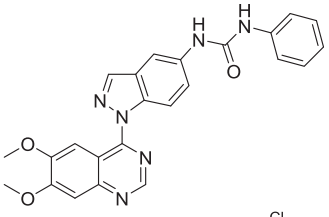	100	83
11b	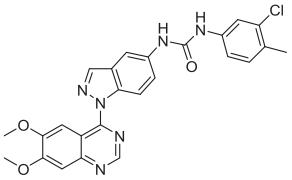	100	5.4
11c	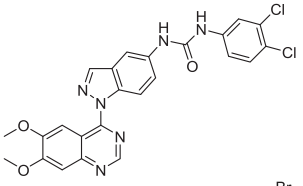	100	5.6
11d	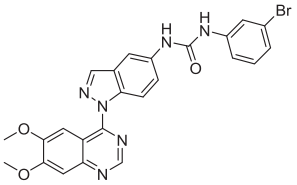	86	NT
11e	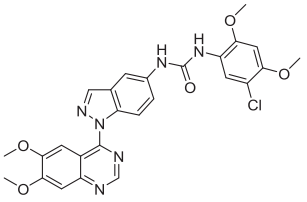	100	7
*Staurosporine (1 μM)[a]		100	NT
Sorafenib[b]		–	90 [12]

NT: not tested.

* In a 96-well plate, each row contains a positive control (no compound) and negative control (background).

[a] Staurosporine was used as a reference in the VEGFR-2 inhibition assay. Staurosporine was also evaluated at 10 nM and 100 nM concentrations, and it showed 85% and 98% inhibition, respectively.

[b] Reported values.

Table 2
HUVEC% proliferation inhibition of compounds **11b** and **11c.**

Compound	HUVEC% inhibition at 10 μM	IC_{50} (μM)
11b	80	NT
11c	99.6	0.0877 ± 0.003
Doxorubicin[a]	84.7	–
Sorafenib	–	0.16 ± 0.01

The experiment was done in absence of the compounds, and the observed growth was considered 100% growth (0%inhibition).

[a] Doxorubicin was used as reference, with IC_{50} = 0.2241 μM. The concentrations used were: 0.01 μM, 0.1 μM, 1μ, and 10 μM.

resistant to VEGFR-2 inhibitory therapy – as previously mentioned [31] – therefore, it is suitable for evaluating the angiogenic independent modes of action of **11c**. The study followed two strategies: 1 – investigating the effect of **11c** on kinases that are downstream of VEGFR-2 and other receptor tyrosine kinases (RTK), 2 – evaluating the proapoptotic effect of **11c**.

2.5. Assessment of the effect on Akt and ERK phosphorylation

Activation of PI3K/Akt pathway is a common feature for cancer progression [83–86]. Upregulation of the mitogen activated protein kinase (MAPK)/ERK pathway is another important feature associated with progression and poor prognosis of cancer. ERK1/2 phosphorylation is often correlated with higher tumor grade of cancer and tumor recurrence [87,88]. Both pathways are known to be downstream for VEGFR-2 and other RTK [89,90].

ELISA assays indicated that treatment of PC-3 cells with compound **11c** significantly reduced Akt phosphorylation by 52.5% ($P < 0.001$) compared to untreated cells. On the other hand, treatment of cells with compound **11c** reduced ERK phosphorylation by 7.9% compared to control, as shown in Fig. 3.

2.6. Effect on caspase-3 activity

The PI3K/Akt pathway also plays a key role in cell survival and resistance to apoptosis [91]. Therefore the compound **11c** was tested for its pro-apoptotic effects. Caspase-3 activation is a final common step for caspase-cascade activation through both the intrinsic and the extrinsic pathways. Its activation ultimately leads to apoptosis therefore it is known as the key executioner of apoptosis [92,93].To assess the pro-apoptotic effects of the tested compounds the activity of caspase-3 was evaluated in the collected cell lysates. Treatment of PC-3 cells with compound **11c** significantly ($P < 0.0001$) boosted caspase-3 activity by 3 folds compared to control indicating that it possesses a proapoptotic activity (Fig. 4).

The aforementioned data indicated that the antiproliferative effect of compound **11c** is at least partly due to its inhibitory effect on Akt. Additionally, compound **11c** exhibited pro-apoptotic activity as evidenced by the increased level of active caspase-3. Further investigation of the full biological profile of **11c** is one of our future perspectives.

2.7. Methods and computational details

2.7.1. Docking simulations against the DFG-out and DFG-in protein conformations

Molecular docking calculations were carried out using the most recent version of smina [94], a version of AutodockVina that offers better control on docking and scoring parameters [95]. Two X-ray crystal structures have been selected to carry out the docking simulations, PDB codes: 4ASE [33] and 3WZD [96]. These two structures were selected particularly because of being with high resolution and for having a smaller number of missing residues than other crystal structures (see supporting info table, S1). The first crystal structure

Table 3
Percent inhibition of the growth of NCI 60 cancer cell lines exerted by final compounds (**11a,** and **11c**) at concentration of 10 μM.

Compound/NSC no Cell name	*11a 781,954*	*11c 781,956*
Leukemia		
CCRF-CEM	77	78
HL-60(TB)	116	85
K-562	61	89
MOLT-4	96	91
RPMI-8226	84	100
SR	73	90
Non-Small Cell Lung Cancer		
A549/ATCC	76	100
EKVX	102	116
HOP-62	–	–
HOP-92	120	157
NCI-H226	114	163
NCI-H23	97	154
NCI-H322M	69	146
NCI-H460	73	154
NCI-H522	80	99
Colon Cancer		
COLO 205	–	–
HCC-2998	66	85
HCT-116	94	76
HCT-15	79	136
HT29	71	117
KM12	95	100
SW-620	50	132
CNS Cancer		
SF-268	78	135
SF-295	73	167
SF-539	99	171
SNB-19	55	90
SNB-75	112	158
U251	–	–
Melanoma		
LOX IMVI	98	178
MALME-3 M	114	144
M14	93	141
MDA-MB-435	68	131
SK-MEL-2	104	127
SK-MEL-28	115	171
SK-MEL-5	60	183
UACC-257	71	110
UACC-62	76	169
Ovarian Cancer		
IGROV1	94	158
OVCAR-3	64	165
OVCAR-4	93	132
OVCAR-5	75	133
OVCAR-8	50	97
NCI/ADR-RES	61	131
SK-OV-3	96	125
Renal Cancer		
786–0	72	143
A498	133	123
ACHN	83	162
CAKI-1	84	91
RXF 393	184	187
SN12C	96	96
TK-10	141	114
UO-31	144	117
Prostate Cancer		
PC-3	118	157
DU-145	89	98
Breast Cancer		
MCF7	120	135
MDA-MB-231/ATCC	108	174
HS 578 T	119	105
BT-549	75	127
T-47D	107	101
MDA-MB-468	167	171
MEAN % Growth inhibition	93	130

Table 4
Five dose assay results obtained for compounds **11a** and **11c** upon testing against the 60 cancer cell lines of NCI screening program (the values are given by μM).

Cell Name	11a			11c		
	GI_{50}	TGI	LC_{50}	GI_{50}	TGI	LC_{50}
Leukemia						
CCRF-CEM	2.56	13.6	55.5	4.01	42.3	> 100
HL-60(TB)	1.57	4.52	16.6	4.44	85.0	> 100
K-562	2.86	15.5	45.5	3.02	10.8	> 100
MOLT-4	0.86	3.56	20.2	2.04	11.4	> 100
RPMI-8226	0.94	12.0	86.1	2.11	7.52	> 100
SR	2.03	15.3	89.0	2.75	> 100	> 100
Non-Small Cell Lung Cancer						
A549/ATCC	1.79	8.74	35.2	2.69	5.75	18.2
EKVX	1.59	7.30	30.5	3.06	9.84	33.3
HOP-62	1.30	10.0	35.1	1.91	3.76	7.41
HOP-92	0.707	4.15	21.7	1.92	4.18	9.13
NCI-H226	1.07	4.06	33.5	2.44	4.80	9.43
NCI-H23	1.30	4.40	32.0	1.93	4.24	9.33
NCI-H322M	0.741	11.4	37.5	2.23	5.47	23.0
NCI-H460	0.706	16.4	94.7	2.08	4.57	10.2
NCI-H522	0.527	2.39	NT	2.50	5.99	29.0
Colon Cancer						
COLO 205	1.32	4.53	18.9	2.32	5.58	47.0
HCC-2998	1.88	11.2	37.7	2.61	8.87	44.3
HCT-116	1.41	4.82	19.4	2.80	10.3	58.4
HCT-15	0.579	11.1	43.0	1.93	4.87	55.9
HT29	0.615	10.9	33.0	1.98	4.29	9.31
KM12	0.207	5.27	78.3	0.05	9.66	> 100
SW-620	3.07	17.9	60.8	2.26	4.76	> 100
CNS Cancer						
SF-268	1.55	11.2	69.1	2.44	7.32	26.5
SF-295	0.73	5.87	26.7	1.38	2.94	6.29
SF-539	0.23	17.3	> 100	0.612	2.47	6.58
SNB-19	2.29	17.7	74.1	2.66	9.58	31.5
SNB-75	0.191	5.69	37.7	1.24	3.41	9.32
U251	1.27	3.23	8.18	1.50	3.06	6.21
Melanoma						
LOX IMVI	0.723	2.75	8.76	1.97	3.76	7.17
MALME-3M	0.502	2.55	NT[b]	1.72	3.89	8.79
M14	1.10	4.22	18.6	1.65	3.58	7.77
MDA-MB-435	1.40	33.9	> 100	1.84	4.29	10.0
SK-MEL-2	1.34	3.52	9.24	2.31	5.01	12.6
SK-MEL-28	1.38	4.33	> 100	1.57	3.24	6.70
SK-MEL-5	5.22	21.3	60.6	2.09	3.88	7.21
UACC-257	2.32	5.13	18.0	3.23	6.79	26.3
UACC-62	1.23	6.27	87.4	1.70	3.44	6.94
Ovarian Cancer						
IGROV1	0.427	4.62	59.7	2.05	4.66	13.4
OVCAR-3	2.08	13.1	40.6	1.92	3.70	7.11
OVCAR-4	1.01	4.25	28.7	1.92	3.89	7.90
OVCAR-5	1.24	13.8	77.2	1.83	4.31	10.7
OVCAR-8	5.17	28.3	> 100	2.77	7.07	48.6
NCI/ADR-RES	2.52	17.6	73.9	2.36	6.23	> 100
SK-OV-3	0.42	4.6	25.6	2.04	4.03	7.99
Renal Cancer						
786-0	1.30	4.34	19.1	1.56	3.52	7.95
A498	0.21	0.896	11.7	2.37	6.24	23.4
ACHN	1.63	11.1	36.2	1.45	3.25	7.27
CAKI-1	2.08	12.1	51.3	2.30	5.94	25.0
RXF 393	1.04	2.76	7.34	1.53	3.29	7.06
SN12C	1.14	5.78	> 100	2.10	4.78	13.5
TK-10	0.724	2.56	7.43	2.38	6.45	31.4
UO-31	0.499	2.84	16.5	2.04	4.17	8.55
Prostate Cancer						
PC-3	1.09	3.36	10.7	1.55	3.24	6.76
DU-145	0.867	11.4	75.4	3.20	11.9	> 100
Breast Cancer						
MCF7	0.234	1.90	> 100	1.85	4.56	> 100
MDA-MB-231/ATCC	1.39	4.92	58.1	1.96	4.03	8.32
HS 578T	0.299	3.37	> 100	2.0	7.95	> 100
BT-549	1.55	12.0	41.1	1.97	4.17	8.83
T-47D	0.183	1.37	43.0	2.39	7.17	67.3
MDA-MB-468	1.18	3.35	9.51	2.17	4.52	9.41

Table 4 (*continued*)

[a]Underlined values of GI_{50} refer to superior potency to sorafenib. Underlined values of LC_{50} refer to superior safety to sorafenib.
[b] NT = not tested.

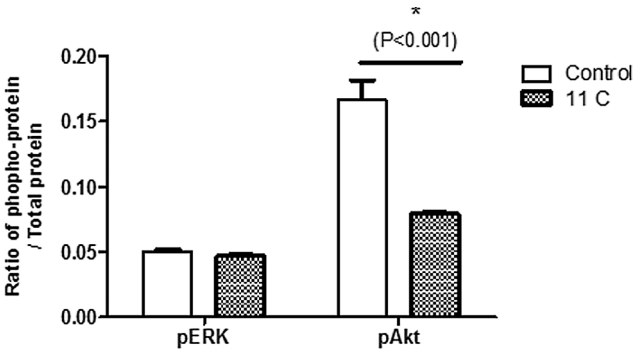

Fig. 3. Effect of compounds **11c** on Akt (a) and ERK (b) phosphorylation and activation using ELISA.

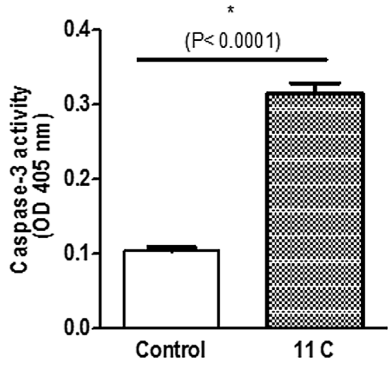

Fig. 4. Effect of compound **11c** on caspase-3 activity in PC-3 prostate cancer cells. Data are mean ± SD, (n = 3).

represents a DFG-out conformation of VEGFR-TK bound to Tivozanib (PDB code: 4ASE) [33], whereas the second crystal structure represents a DFG-in conformation of VEGFR-TK bound to Lenvatinib (PDB code: 3WZD) [96]. The two crystal structures were first downloaded from the protein data bank and prepared using the protein preparation wizard in the Schrodinger software package [42]. Ligand atoms were deleted and missing atoms were added and titrable groups were adjusted at a pH of 7. Protein structures were then saved as PDB files and converted to PDBQT files and used as inputs for smina. Ligand structures were prepared using the ligprep [97] module of Schrodinger and saved as mol2 files for use in smina. In addition to the 16 novel inhibitors under investigation, we have also included 5 known VEGFR-2-TK crystallized ligands to be used as a benchmarking set to our novel inhibitors and to assess the performance of our computational protocol. These ligands are Lenvatinib (PDB code: 3WZD) [96], Sorafenib (PDB code: 3WZE) [96], Tivozanib (PDB code: 4ASE) [33], a naphthamide inhibitor (PDB code: 3B8Q) [53] and a benzoxazine inhibitor (PDB code: 2RL5) [98]. For simplicity, these ligands will be denoted as LEN, SOR, TIV, NAP and BEN, respectively. With the exception of LEN that targets a DFG-in conformation of VEGFR-2-TK, all other ligands are known to target a DFG-out conformation.

The search space was limited to a 20 * 20 * 20 $Å^3$ box around the original ligand-binding site with and an exhaustiveness search parameter of 20 (default is 8). The best 3 scoring poses for each ligand were selected and visually inspected for a proper filling of the designated binding site. Poses that do not satisfy proper interaction with the hinge residue, Cys919, were discarded. If none of the best three poses exhibits the Cys919, we continue our search until a proper pose is found. Successful poses were subjected to molecular dynamics (MD) simulations and binding free energy calculations using the AMBER-MMGBSA module [99]. Unless otherwise stated, only the top AMBER-MMGBSA pose is reported.

2.7.2. Molecular dynamics simulations and binding free energy estimation

Simulated protein-ligand complexes were prepared with tleap using the AMBER-FF99SB [100] forcefield for the protein and the GAFF forcefield for the ligands [101]. Missing ligand charges were calculated using the AM1-BCC method of antechamber [102]. Each complex was then immersed in a cubic 12 $Å^3$ box of TIP3 water and neutralized with counter ions and put to a 150 mM salt concentration by adding the proper number of Na+ and Cl− ions. Each system was then subjected to several rounds of minimization and equilibration simulations. Initially, 20,000 steps of energy minimizations were conducted in four consecutive rounds in which ligands and protein atoms are constrained to their original 3D coordinates and constrains are gradually relieved from 100, 50, 5, 1 kcal/mol. This was followed by a non-constrained energy minimization for 5000 steps. Each system was then brought to 300 K by a gradual heating NVT simulation over a 50,000 steps constrained simulation. This was followed by 4 constrained NPT equilibration simulations of 25,000 steps in which protein constrains were gradually reduced from 5, 1, 0.1 and 0.01 kcal/mol constrains followed by a final 25,000 steps un-constrained equilibration simulation. Production simulations were carried out for 5 * 1 ns simulations and trajectories were merged at the end to give a single 5 ns MD simulation trajectory. Periodic boundary conditions and an integration time step of 1 fs were used for all simulations. Long-range electrostatic interactions were computed using the Particle Mesh Ewald summation method [103] and the short-range electrostatic interactions were truncated after 9 Å. The binding free energies were calculated using the AMBER-MMGBSA module and averaged over the 5 ns simulation trajectories. MD simulations were carried out using the GPU implementation of pmemd (pmemd.cuda) of the most recent version of AMBER bio-molecular simulation software.

2.7.3. The binding modes of the novel inhibitors compared to known VEGFR-TK ligands

In the current study and as we were interested to determine the targeted conformations by our novel compounds, two X-ray crystal structures have been selected to predict the binding modes. Each structure typifies a distinct conformation of the VEGFR-2 catalytic domain. The first structure, PDB code: 3WZD represents an active DFG-in conformation, whereas the second structure, PDB code: 4ASE represents an inactive DFG-out conformation of the VEGFR-2 catalytic domain. Fig. 5 displays the structure of the DFG-in conformation, PDB code: 3WZD, whereas Fig. 6 displays a structure for the DFG-out conformation, PDB code: 4ASE, with the co-crystallized ligands Lenvatinib (LEN) and Tivozanib (TIV), respectively. As we can see in the figures, LEN binds to the DFG-in conformation and forms a strong H-bond with the hinge residue Cys919 backbone amide group and extends only partially to the side pocket. On the other hand, TIV forms H-bond with the hinge residue Cys919, extends the bulky phenyl-methylisoxazol group deeply into the side hydrophobic pocket and interacts with side pocket lipophilic residues, such as Ile888, Ile892, Val898, Leu1019 and Ile1044. Both ligands also form additional H-bonds with Asp1046 and Glu885 in the side pocket through their urea motif.

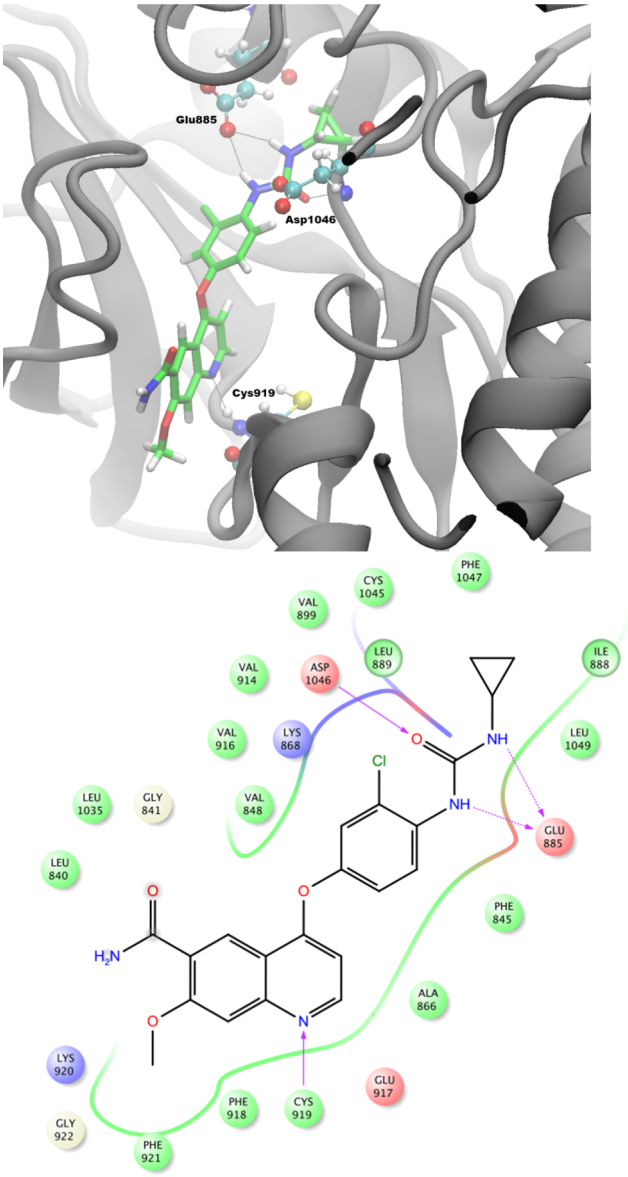

Fig. 5. The (a) 3D and the (b) 2D ligand interaction of LEN bound to the DFG-in conformation of the VEGFR-2 catalytic domain (PDB code: 3WZD). LEN forms a very strong H-bond interaction with Cys919 in addition to Glu885 and Asp1046.

To gain more insight into the atomistic details of the interaction of the novel inhibitors in comparison with known VEGFR-2 TK binders, we have given the three-dimensional (3D) and the two-dimensional (2D) ligand interaction diagrams for the most three active inhibitors tested *in vitro*, compound **11b** (IC_{50} 5.4 nm), compound **11c** (IC_{50} 5.6 nm) and compound **11e** (IC_{50} 7 nm) in Fig. 7. As expected and being bulky, these inhibitors seems to exclusively target the DFG-out conformations of VEGFR-2-TK. All inhibitors are able to interact very strongly with the hinge residue, Cys919. The urea moieties in the side group are capable of forming very productive H-bonding interactions with the main chain amide nitrogen of Asp1046 and the side chain of Glu885. The substituted chloro-phenyl ring extends deeply in the hydrophobic pocket forming additional lipophilic interactions with nearby hydrophobic residues, such as Ile889, Ile892 and Leu1019.

To assess the stability of the generated complexes during the MD simulation, the RMSD for the protein Cα and ligands heavy atoms of the

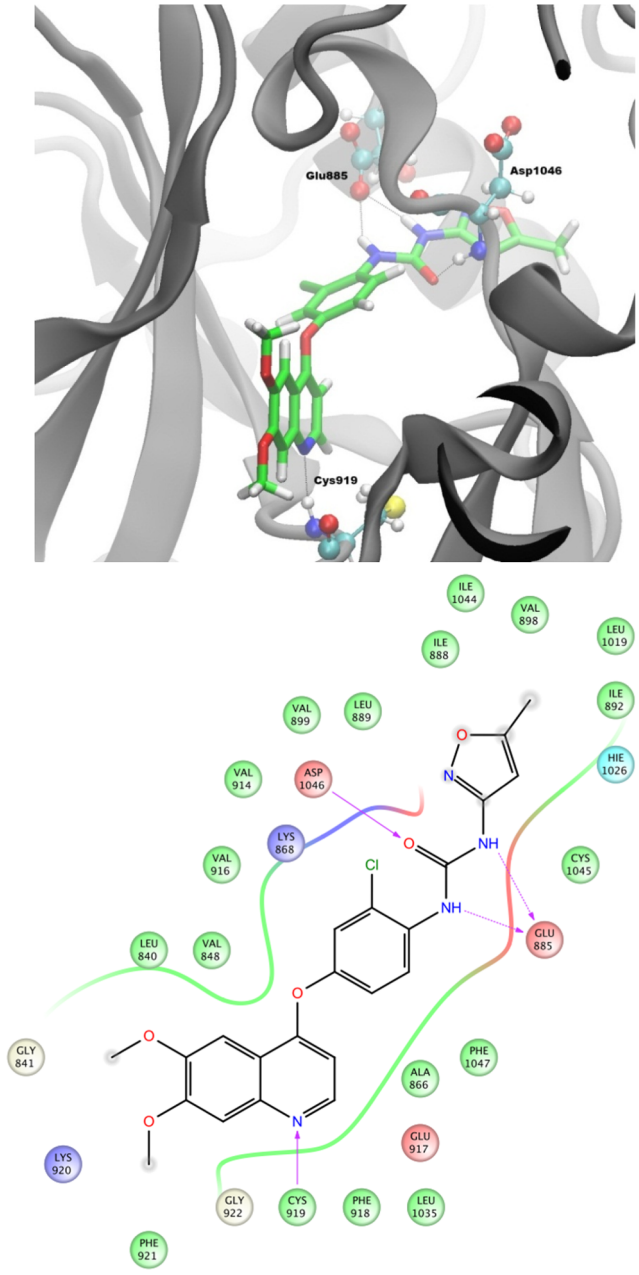

Fig. 6. The (a) 3D and the (b) 2D ligand interaction of TIV bound to the DFG-out conformation of the VEGFR-2 catalytic domain (PDB code: 4ASE). TIV forms a very strong H-bond interaction with Cys919 in addition to Glu885 and Asp1046.

protein ligand complexes formed with compounds **11b, 11c**, **11e**, and **7c** (one of the weakest inhibitors) have been calculated over the 5 ns MD trajectory. Protein atoms reach a stable MD trajectory in the first 0.5 ns of the simulation with minimal fluctuations after that with an average RMSD value of approximately 2.0 Å. Maximum RMSD fluctuations is reached by the Cα atoms of complex formed with compound **7c** which reaches a maximum of 2.7 Å. In contrast to the relatively stable RMSD trajectories for the protein atoms, RMSD values for ligand atoms show obvious variations between the most active compounds that are compounds **11b**, **11c** and **11e** and the weak inhibitor, compound **7c**. Also, the ligands atoms of compounds **11b**, **11c** and **11e** exhibit very stable RMSD values of below 1.0 Å in contrast to the atomic RMSD value of compound **7c**, which displays an average RMSD value of approximately 1.7 Å and a maximum of 2.2 Å (see supplementary).

2.7.4. Structure activity relationship

Based on the exceptionally high potency of the three most potent derivatives, compound **11b** (IC_{50} 5.4 nm), compound **11c** (IC_{50} 5.6 nm) and compound **11e** (IC_{50} 7 nm), three main conclusions can be drawn. First, it seems that an optimum size of substituents on the terminal phenyl ring provides the best overall potency for the inhibitors to reach the single digit nanomolar range. For example, chlorine-substituted aryl derivatives exhibit much higher potencies than bromine-substituted derivatives in the non-N—H linker containing derivatives. Typical examples are compounds **11b** (IC_{50} 5.4 nm) and **11c** (IC_{50} 5.6 nm) that show 100% inhibition of enzymatic activities at 10 μM compared to **11d**, which shows 86% inhibition at the same concentration. Also, the unsubstiuted phenyl ring in **11a**, results in a significantly lower IC_{50} value of 83 nm compared to compounds **11c** and **11b**. The second conclusion is that the presence of the N—H linker significantly reduces the activity, presumably due to entropic reasons. In other words, the conformational constraint introduced by the direct attachment of the indazolyl group enhances the potency of the compounds. This is typically the case when a derivative from the N—H linker containing derivatives, such as compound **8b** (48% inhibition), compound **8a** (100% inhibition, IC_{50} 148 nm) and compound **8d** (50% inhibition) are compared with their corresponding non-N—H linker containing analogues, which are compound **11b** (100% inhibition, IC_{50} 5.4 nm), compound **11c** (100% inhibition, IC_{50} 5.6 nm) and compound **11e** (100% inhibition, IC_{50} 7 nm), respectively. Herein, an important conclusion can be drawn. In most reported VEGFR-2 type II inhibitors NH-linker-based derivatives exhibited mediocre activity profiles, as compared with the O-linker-based ones, where using O-linker increased activity by several folds [53,58,59,61,104–106]. Our second rigidification strategy represents another option for promoting activity, in addition to using O-linker.

Another very interesting observation was the significance of the presence of a 6,7-di-substituted quinzaoline ring. As discussed in earlier studies for VEGFRs TKIs as well as other TKIs, the presence of these 6,7-di-substituted quinazoline tails stabilizes the formed protein-ligand complexes, presumably through a pushing effect on the ligand to tightly pack the side hydrophobic pocket [104,107–109]. We have examined this hypothesis for our new derivatives by monitoring the MD simulation to see if the absence of these tails will disturb the formed complexes. Indeed for the complexes formed by compounds **7a-d** that lack the 6,7-quinazoline tails, we observed that during the MD simulations, the ligands partially migrate from the binding pocket, loosening the very important anchoring H-bond with the hinge residue, Cys919 (see supplementary file for examples). To quantify this behavior, we have calculated the % occupancy of the H-bond formed by the quinazoline nitrogen with Cys919 during the 5 ns MD for all inhibitors under study. Percentage occupancy values are given in Table 5 together with the binding energies as well as the *in vitro* assay data. As we can see in the table, all inhibitors that lack the 6,7-quinazoline tails have significantly lower occupancies for this Cys919 H-bond compared to their tail containing analogues. For example, the % occupancy of this H-bond for compound **7a** (−4% inhibition) is given by 0.44%, for compound **7d** (10% inhibition) is given by 0.24%, for compound **7b** (7% inhibition) is given by 1.60% and for compound **7c** (4% inhibition) is given by 0.44%. It is noteworthy to mention here that we also examined other poses with higher binding energies for these compounds to make sure that this phenomenon is not an artifact of the simulation and we observed the same behavior. In contrast to this very low occupancy values of the weak inhibitors, **7a-d** for H-bonding with Cys919, we have examined the occupancy values for the strong inhibitors and we indeed found that potent inhibitors enjoys a very high occupancy values. For example, the most active inhibitors **11b**, **11c** and **11e** exhibit occupancies of 88.4%, 87.88% and 95.52%, respectively. The table also gives the occupancy values for the H-bond formed with Asp1046. Nevertheless, based on the data listed on the table, it can be concluded that the occupancy values of this H-bond plays a much less critical role in determining the activity of the compounds.

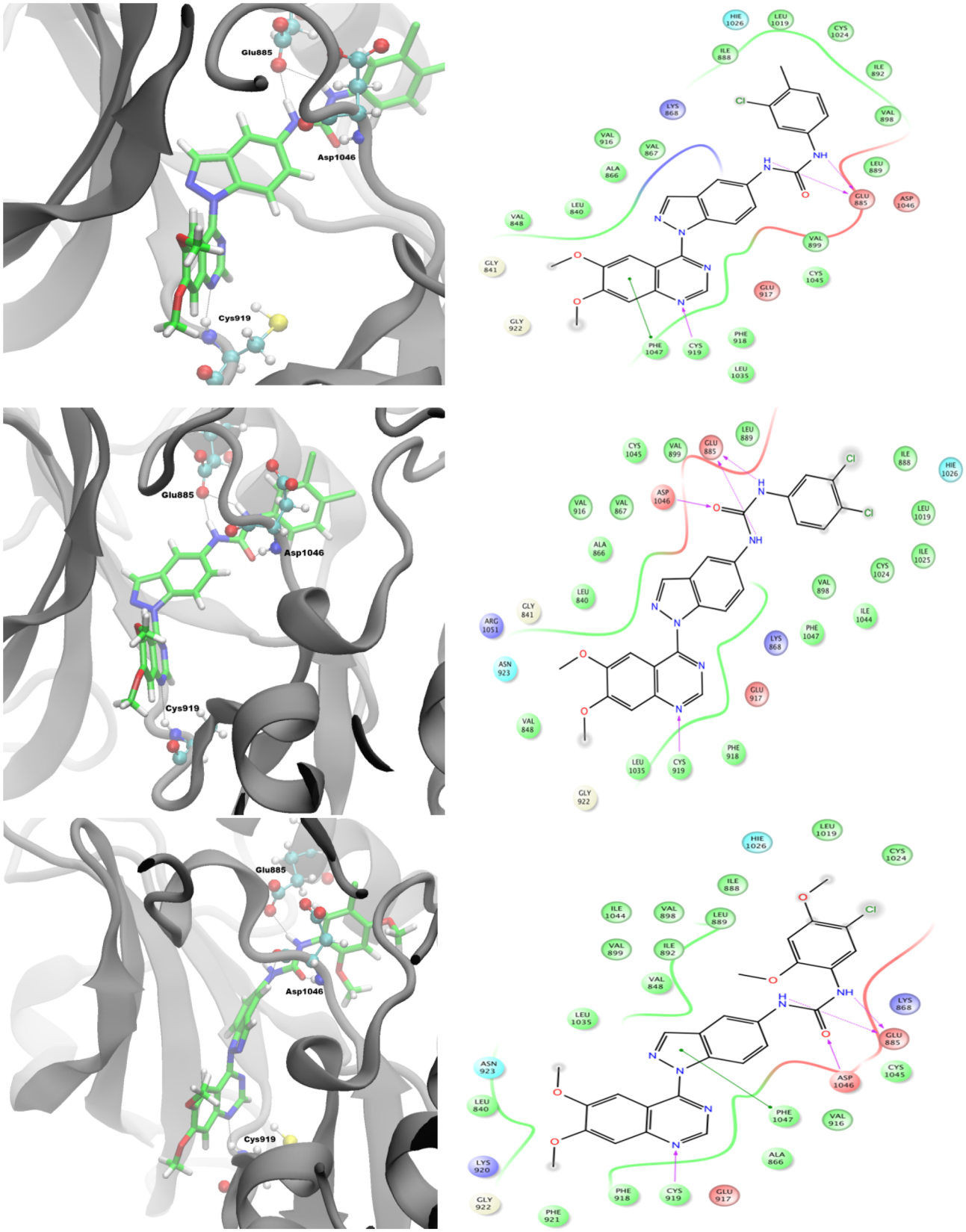

Fig. 7. The 3D and 2D ligand interaction diagrams of compounds 11b (upper panel), compound 11c (middle panel) and compound 11e (lower panel) bound to the DFG-out conformation of VEGFR2 TK domain. All inhibitors are capable of forming strong interaction.

Table 5
The complete list of compounds studied with their calculated AMBER-MMGBSA binding energies, important H-bond %occupancies as well as the *in vitro* measured % inhibition at 10 μM and and the IC_{50} values. The table also gives the Pearson correlation of the calculated binding energies and the IC_{50} data, which is given by 0.64. With the exception of LEN and **5**, which are predicted to bind to the DFG-in conformation 3WZD crystal structure, all other inhibitors are predicted to bind to the 4ASE that typifies a DFG-out conformation [7,110–113].

Compound name	Binding energy	Cys919 H-bond occupancy (%)	Average Cys919 H-bond (Ang.)	Asp1046 H-bond occupancy (%)	Average Asp1046 H-bond (Ang.)	IC_{50} (nM)	% Inhibition at 10 μM
NAP[1]	−58.23	97.44	3.059	99.24	2.936	0.5	–
BEN[2]	−56.97	97.44	3.058	99.52	2.934	0.5	–
11e	−52.72	95.52	3.103	99.96	2.817	7	100
8d	−48.26	95.72	3.133	100	2.852	–	50
8a	−49.83	94.44	3.14	100	2.822	148	100
TIV[3]	−52.48	95.04	3.067	96.4	2.968	0.16	–
8b	−48.35	63.6	3.118	99.88	2.856	–	48
11c	−47.71	87.88	3.107	84.96	2.98	5.6	100
11a	−46.95	95.76	3.133	99.96	2.872	83	100
SOR[4]	−46.17	87.6	3.213	99.2	2.904	90	–
8c	−43.10	96.44	3.109	97.48	2.897	–	86
11b	−45.86	88.4	3.126	62.0	3.011	5.4	100
11d	−42.26	67.92	3.141	60.6	3.109	–	86
LEN[5]	−48.79	95.04	3.089	98.44	2.894	4	–
7a	−42.49	0.44	3.41	99.84	2.893	–	−4
7b	−39.44	1.6	3.385	99.56	2.951	–	7
7d	−39.66	2.96	3.136	98.68	2.872	–	10
8f	−37.49	98.0	3.11	94.8	3.195	163	100
7c	−35.54	0.44	3.149	97.8	2.9	–	4
8e	−38.46	2.08	3.084	97.04	2.98	–	94
5	–22.46	26.76	3.305			–	6
$r_{Pearson}$ with IC_{50}	0.64						

2.7.5. The AMBER-MMGBSA binding energies of the novel inhibitors and the known ligands

Table 5 also lists the calculated AMBER-MMGBSA binding energy data for the new inhibitors under study as well as the known VEGFR-2 TKIs ligands. Including these known ligands in our calculations was very important to act as positive controls for the new inhibitors and to benchmark the results. It is noteworthy to mention here that the high flexibility of VEGFR-2 TKIs implies that in addition to considering the binding affinity of the ligands to the target in order to quantify the potency, it is also important to take binding kinetics measures into account. Examples of these measures to determine the binding kinetics is the residence time (mins), the association (k_{on}, S^{-1} M^{-1}) and dissociation (k_{off}, S^{-1}) rate constants. This is different from the other more commonly used equilibrium constants, such as the equilibrium dissociation constant K_d (nmol/L) or IC_{50} values that are typically used as measures of drug potency. In the current study, we will consider the IC_{50} values as the main measure for drug potency to be correlated with the calculated binding energies.

As can be seen in Table 5, the AMBER-MMGBSA data achieves a good correlation ($r_{pearson}$ = 0.64) with the *in vitro* measured IC_{50} values for the compounds. All known VEGFR-2 TKIs exhibit low binding energies with NAP and BEN have the lowest binding energies among the whole list of inhibitors under investigation, with values given by −58.23 kcal/mol and −56.97 kcal/mol, respectively. Compound **11e**, the third most potent compound in our novel series of compounds (100% inhibition, IC_{50} = 7 nM), exhibits the lowest binding energy in our series, −52.72 kcal/mol. Also, very weakly active compounds, exhibit very poor binding energies as well. For example, compound **7c** (4% inhibition exhibits the highest binding energy among the whole list of studied inhibitors, that is −35.54 kcal/mol. However, binding energy failed to correlate with the activity of some compounds such as **7a**, **8b**, and **8d**. On the other side, the occupancy of Cys919 H- bond was better correlated with the activity, highlighting its pronounced effect on VEGFR-2 inhibitory action.

3. Conclusion

Two series of indazole-based compounds were designed, synthesized and biologically evaluated, using two different conformational restriction strategies. The second design strategy yielded more active compounds that act as type II kinase inhibitors, supporting the rationale of the design. Compounds **11b, 11c** and **11e** were the most active compounds with IC_{50} of 5.4, 5.6 and 7 nM respectively. Molecular dynamics study were made to illustrate the difference in behaviour between the most active compounds **11b, 11c** and **11e** and one of the weakest inhibitors **7c**. Compound **7c** showed high RMSD values for the ligand atoms in comparison to the low RMSD values for compounds **11b, 11c** and **11e**. Also, the dynamics study showed the effect of 6,7-disubstitution on quinazoline ring. It demonstrated that this disubstitution that extend to the solvent accessible area stabilized the compound in the binding site and increased the % occupancy of the essential hydrogen bond with Cys919. Additionally, this work supports a relatively novel design strategy for VEGFR-2 inhibitors that avoids using the unfavourable NH linker. Instead the linker is included in a ring, yielding a less flexible structure. In Fig. 8, we introduce a graphical representation of the SAR of the most potent series in this work **11a-e.**

In order to assess the *in vitro* cellular antiangiogenic activity, compounds **11b** and **11c** were tested against HUVEC cell line, where they showed 80% and 99.6% inhibitory activity respectively.

In vitro anticancer activity was evaluated for 4 compounds selected by NCI. Compounds **11a** and **11c** showed remarkable mean % GI against NCI-60 panel of cell lines of 93% and 130%, respectively, and they were selected for further five-dose evaluation. As compared to sorafenib, both compounds showed superior potency and safety profiles against numerous cell lines. Further investigation of the underlying mechanism of *in vitro* antiproliferative action demonstrated that the mechanism is a combination of VEGFR-2 kinase inhibition, interfering with the downstream AKT pathway, and induction of apoptosis through the action on caspase-3.

In brief, in this work, conformational restriction was employed to develop a potent VEGFR-2 inhibitor: **11c** (IC_{50} = 5.6 nM), that can exert anticancer activity through angiogenesis-dependent and independent modes of action, with reasonable safety. Computational methods were implemented to develop SAR of the synthesized compounds, which can facilitate future optimization. Thus, **11c** is a suitable candidate for further development and preclinical studies.

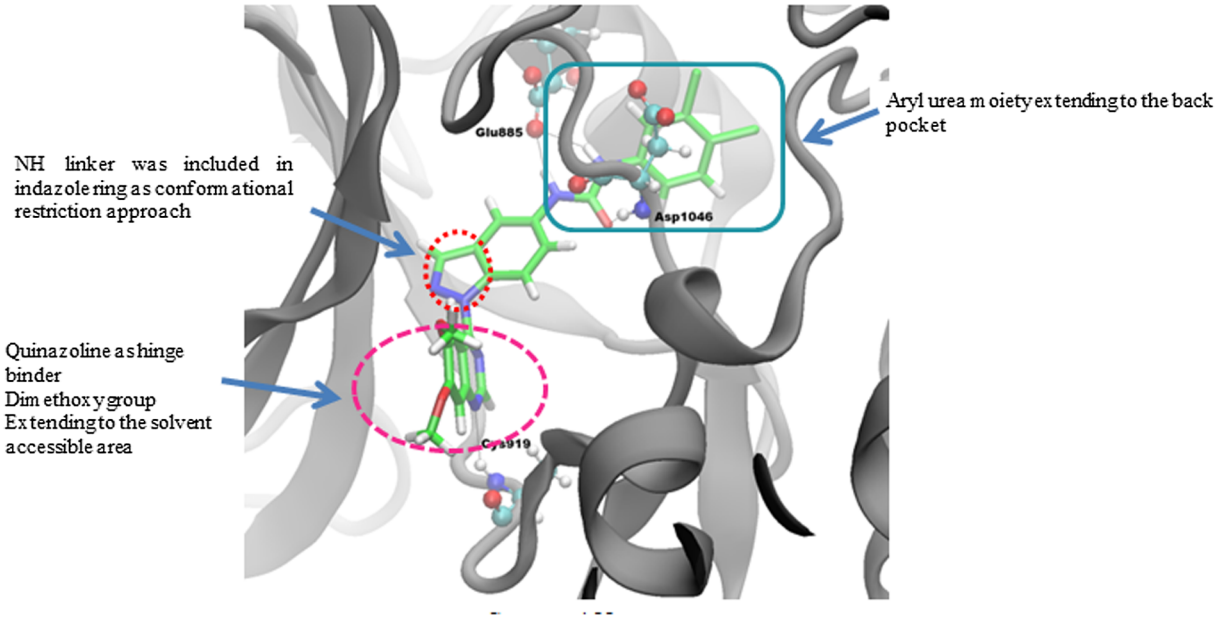

Fig. 8. SAR representation of our novel series of compounds. The figure shows **11c** in the binding site of VEGFR-2 kinase.

4. Experimental

4.1. Chemistry

All chemicals used were purchased from Aldrich (USA), Alfa-Aesar Organics (USA) and SD-fine (India) and used without further purification. Melting points determined in one end open capillary tubes using Stuart Scientific apparatus and were uncorrected. ^{1}HNMR spectra were recorded in δ scale given in ppm on a Joel 300 MHz or 400 MHz spectrophotometer and referred to TMS at Microanalytical Center at Cairo University or the faculty of Pharmacy, Cairo University respectively. ^{13}C spectra were run at 126 MHz in dimethylsulfoxide (DMSO-d_6). Chemical shifts are quoted in **δ** and were related to that of the solvents at Microanalytical Center at Cairo University. Analytical thin layer chromatography (TLC) was performed on silica gel 60 F_{254} packed on Aluminium sheets, purchased from Merck (Merck, Darmstadt, Germany), the developing solvents were DCM/MeOH (9:1), with visualization under U.V. light (254 nm). FT-IR spectra were recorded on a Perkin-Elmer spectrophotometer (Ain Shams University). Elemental analyses were performed at Al-azhar university.

Compounds **2**, **3** and **4** were prepared according to the procedures reported in the literature [69,114,115].

4.1.1. 5-((2-Chloropyrimidin-4-yl)amino)-N-phenyl-1H-indazole-1-carboxamide (5)

To a solution of **4** (0.2 g, 0.814 mmol) in dry THF (15 mL) phenyl isocyanate (0.097 g, 0.814 mmol) was added. The resulted solution was stirred at room temperature for 24 h, then, solvent was removed under vacuo and resulting solid was washed thoroughly with methanol and diethyl ether to give the titled compound as pale pink powder (148 mg, 49.84%). m.p.: > 250 °C, ^{1}H NMR (300 MHz, DMSO-d_6) δ 10.34 (s, 1H, NH), 10.29 (s, 1H, NH), 8.58 (s, 1H, ArH), 8.32 (s, 1H, ArH), 8.26 (d, J = 9, 1H, ArH), 8.19 (d, J = 5.9, 1H, ArH), 7.80 (d, J = 8.5, 2H, ArH), 7.65 (d, J = 9, 1H, ArH), 7.39 (t, J = 8.5, 2H, ArH), 7.15 (t, J = 8.5, 1H, ArH) 6.82 (d, J = 5.9, 1H, ArH), Anal. Calcd for $C_{18}H_{13}ClN_6O$: C, 59.27; H, 3.59; N, 23.04, Found: C, 59.42; H, 3.63; N, 23.17.

4.1.2. General procedure for preparation of target compounds (6a) and (6b)

Mixture of 5-aminoindazole **3** (1 g, 7.51 mmol) and the appropriate quinazoline derivative (7.51 mmol) in isopropanol (38 mL) was refluxed for 3 h, where a heavy yellow ppt of HCl salt of the product was formed. The mixture was, then, cooled to r.t., filtered and the ppt. was washed thoroughly with isopropanol and ether and heated with mixture of 65 mL of water and ethanol with ratio (4:1) that was basified with aqueous ammonia. Mixture was cooled and filtered to yield the product that was washed with water and dried.

*4.1.2.1. N-(1H-indazol-5-yl)quinazolin-4-amine **(6a)**.* The product was separated as off- white solid, (0.96 g, 48.92%) m.p.: 232–234 °C. ^{1}H NMR (300 MHz, DMSO-d_6) δ 13.19 (s, 1H, NH), 11.18 (s, 1H, NH), 8.82 (d, J = 8.3 Hz, 1H, ArH), 8.76 (s, 1H, ArH), 8.13 (s, 1H, ArH), 8.09–7.98 (m, 2H, ArH), 7.96 (d J = 8.6, 1H, ArH), 7.77–7.63 (m, 2H, ArH), 7.62 (s, 1H, ArH).

*4.1.2.2. N-(1H-indazol-5-yl)-6,7-dimethoxyquinazolin-4-amine **(6b)**.* The product was separated as off- white solid,(1.6 g, 81.54%) m.p.: 266–268 °C. ^{1}H NMR (300 MHz, DMSO-d_6) δ12.99 (s, 1H, NH), 9.50 (s, 1H, NH), 8.40 (s, 1H, ArH), 8.13 (s, 1H, ArH), 8.07 (s, 1H, ArH), 7.87 (s, 1H, ArH), 7.64 (d, J = 8.2, 1H, ArH), 7.55 (d, J = 8.2, 1H, ArH), 7.17 (s, 1H, ArH), 3.96 (s, 3H, OCH_3), 3.93 (s, 3H, OCH_3).

4.1.3. General procedure for the preparation of target compounds (7a–d)

Compound **6a** (0.2 g, 0.765 mmol) was dissolved in dry THF (20 mL), to which isocyanate (0.765 mmol) was added. The mixture was stirred at r.t. for 24 hrs and then, it was filtered and the ppt. was washed with excess THF and ether and dried to give the titled compounds **7a-d.**

*4.1.3.1. N-(3-Chloro-4-methylphenyl)-5-(quinazolin-4-ylamino)-1H-indazole-1-carboxamide **(7a)**.* The product was separated as pale yellow powder. (72 mg, 21.93%) m.p.: 216–218 °C.^{1}H NMR (300 MHz, DMSO-d_6) δ 11.67 (s, 1H, NH), 10.50 (s, 1H, NH), 8.91 (s, 1H, ArH), 8.76 (d, J = 8.3 Hz, 1H. ArH), 8.17 (s, 1H, ArH), 8.16–8.08 (m, 1H, ArH), 8.05 (s, 1H, ArH), 7.95–7.83 (m, 2H, ArH), 7.67 (d, J = 8.6 Hz, 1H, ArH), 7.59 (d, J = 8.9 Hz, 1H, ArH), 7.44 (d, J = 8.1 Hz, 1H, ArH), 7.38 (s, 1H, ArH), 7.21 (d, J = 7.9 Hz, 1H, ArH), 2.32 (s, 3H, CH_3).

*4.1.3.2. N-(3,4-Dichlorophenyl)-5-(quinazolin-4-ylamino)-1H-indazole-1-carboxamide **(7b)**.* The product was separated as white powder. (40 mg, 11.63%) m.p.: 226–229 °C, ^{1}H NMR (300 MHz, DMSO-d_6) δ 11.75 (s, 1H, NH), 10.73 (s, 1H, NH), 8.97 (s, 1H, ArH), 8.78 (d, J = 8.5 Hz, 1H,

ArH), 8.61 (s, 1H, ArH), 8.44 (d, J = 9.0 Hz, 1H, ArH), 8.25 (d, J = 1.5 Hz, 1H, ArH), 8.18 (d, J = 2.3 Hz, 1H, ArH), 8.13 (t, J = 8.3 Hz, 1H, ArH), 7.95–7.88 (m, 3H, ArH), 7.85 (dd, J = 9.0, 2.3 Hz, 1H, ArH), 7.61 (dd, J = 8.9, 1.5 Hz, 1H, ArH).

*4.1.3.3. N-(3-Bromophenyl)-5-(quinazolin-4-ylamino)-1H-indazole-1-carboxamide **(7c)***. The product was separated as pale yellow powder. (109 mg, 31%) m.p.: 214–218 °C, ^{1}H NMR (300 MHz, DMSO-d_6) δ 11.67 (s, 1H, NH), 10.58 (s, 1H, NH), 8.97 (s, 1H, ArH), 8.76 (d, J = 8.5 Hz, 1H, ArH), 8.44 (d, J = 8.7, 1H, ArH), 8.24 (s, 1H, ArH), 8.15–8.04 (m, 2H, ArH), 7.88–7.82 (m, 2H, ArH), 7.60 (d, J = 8.8 Hz, 1H, ArH), 7.63 (d, J = 8.8 Hz, 1H, ArH), 7.40 (d, J = 8.7 Hz, 1H, ArH), 7.25–7.13 (m, 2H, ArH), Anal. Calcd for $C_{22}H_{15}BrN_6O$: C, 57.53; H, 3.29; N, 18.30, Found: C, 57.71; H, 3.25; N, 18.3.9.

*4.1.3.4. N-(5-Chloro-2,4-dimethoxyphenyl)-5-(quinazolin-4-ylamino)-1H-indazole-1-carboxamide **(7d)***. The product was separated as yellow powder. (320 mg, 88%) m.p.: 220–222 °C, ^{1}H NMR (300 MHz, DMSO-d_6) δ 11.66 (s, 1H, NH), 10.50 (s, 1H, NH), 8.88 (s, 1H, ArH), 8.76 (d, J = 8.5 Hz, 1H, ArH), 8.23–7.99 (m, 3H, ArH), 7.97–7.77 (m, 2H, ArH), 7.72–7.50 (m, 2H, ArH), 7.38 (s, 1H, ArH), 6.94 (s, 1H, ArH), 3.98 (s, 3H, OCH_3), 3.92 (s, 3H, OCH_3), Anal. Calcd for $C_{24}H_{19}ClN_6O_3$: C, 60.70; H, 4.03; N, 17.70, Found: C, 60.84; H, 4.07; N, 17.83.

*4.1.4. General procedure for preparation of target compounds **(8a-f)***

Compound **6b** (0.2 g, 0.622 mmol) was dissolved in dry DMF (7.5 mL), to which appropriate isocyanate or isothiocyanate (0.622 mmol) was added. The mixture was stirred at r.t. for 24 h, poured on ice, stirred for 30 min. and filtered. The resulted ppt was washed with acetic acid, then excess water and left to dry, then washed with ether and dried to give the titled compounds **8a-f.**

*4.1.4.1. N-(3-Chloro-4-methylphenyl)-5-((6,7-dimethoxyquinazolin-4-yl) amino)-1H-indazole-1-carboxamide **(8a)***. The product was separated as yellow powder.(50 mg, 16.43%) m.p.: 196–198 °C. ^{1}H NMR (400 MHz, DMSO-d_6) δ 10.58 (s, 1H, NH), 9.81 (s, 1H, NH), 8.58 (s, 1H, ArH), 8.53 (s, 1H, ArH), 8.45 (d, J = 2.1 Hz, 1H, ArH), 8.35 (d, J = 8.9 Hz, 1H, ArH), 8.15 (s, 1H, ArH), 7.92 (d, J = 9 Hz, 1H, ArH), 7.87–7.82 (m, 1H, ArH), 7.34 (s, 1H, ArH), 7.22 (s, 1H, ArH), 7.17 (d, J = 8.0 Hz, 1H, ArH), 3.99 (s, 3H,OCH_3), 3.96 (s, 3H,OCH_3), 1.92 (s, 3H, CH_3). Anal. Calcd for $C_{25}H_{21}ClN_6O_3$: C, 61.41; H, 4.33; N, 17.19, Found: C, 61.59; H, 4.31; N, 17.32.

*4.1.4.2. N-(3,4-Dichlorophenyl)-5-((6,7-dimethoxyquinazolin-4-yl) amino)-1H-indazole-1-carboxamide **(8b)***. The product was separated as yellow powder.(72 mg, 22.71%) m.p.: 202–205 °C . ^{1}H NMR (300 MHz, DMSO-d_6) δ 11.20 (s, 1H, NH), 9.32 (s, 1H, NH), 8.74 (s, 1H, ArH), 8.10 (m, 2H, ArH), 7.96 (s, 1H, ArH), 7.85 (s, 1H, ArH), 7.49–7.18 (m, 4H, ArH), 6.84 (s, 1H, ArH), 3.97 (s, 6H, OCH_3).

*4.1.4.3. N-(3-Bromophenyl)-5-((6,7-dimethoxyquinazolin-4-yl)amino)-1H-indazole-1-carboxamide **(8c)***. The product was separated as pale yellow powder. (48 mg, 14.85%) m.p.: 198–201 °C, ^{1}H NMR (300 MHz, DMSO-d_6) δ 11.22 (s, 1H, NH), 9.05 (s, 1H, NH), 8.78 (s, 1H, ArH), 8.14 (s, 1H, ArH), 8.09 (s, 1H, ArH), 7.98 (s, 1H, ArH), 7.72–7.60 (m, 2H, ArH), 7.53 (d, J = 8.8 Hz, 1H, ArH), 7.49–7.33 (m, 1H, ArH), 7.29 (s, 1H, ArH), 7.25–7.13 (m, 2H, ArH), 3.99 (s, 6H, OCH_3). Anal. Calcd for $C_{24}H_{19}BrN_6O_3$: C, 55.50; H, 3.69; N, 16.18, Found: C, 55.61; H, 3.68; N, 16.41.

*4.1.4.4. N-(5-Chloro-2,4-dimethoxyphenyl)-5-((6,7-dimethoxyquinazolin-4-yl)amino)-1H-indazole-1-carboxamide **(8d)***. The product was separated as white powder. (35 mg, 10.51%) m.p.: 226–228 °C, ^{1}H NMR (300 MHz, DMSO-d_6) δ 11.21 (s, 1H, NH), 9.46 (s, 1H, NH), 8.85 (s, 1H, ArH), 8.54 (s, 1H, ArH), 8.32 (s, 1H, ArH), 8.17 (s, 1H, ArH), 8.13–8.01 (m, 2H, ArH), 7.80 (s, 1H, ArH), 7.33–7.21 (m, 1H, ArH), 6.90 (s, 1H, ArH), 4.15–3.81 (m, 12H, OCH_3). Anal. Calcd for $C_{26}H_{23}ClN_6O_5$: C, 58.38; H, 4.33; N, 15.71, Found: C, 58.54H, 4.37; N, 15.87.

*4.1.4.5. 5-((6,7-Dimethoxyquinazolin-4-yl)amino)-N-phenyl-1H-indazole-1-carboxamide **(8e)***. The product was separated as off-white powder. (52 mg, 18.97%) m.p.: 216–218 °C, ^{1}H NMR (300 MHz, DMSO-d_6) δ 11.10 (s, 2H, NH), 8.59 (s, 1H, ArH), 8.09 (s, 1H, ArH), 8.02 (s, 1H, ArH), 7.92 (s, 1H, ArH), 7.59 (d, J = 8.7 Hz, 1H, ArH), 7.49 (d, J = 8.9 Hz, 1H, ArH), 7.42–7.20 (m, 5H, ArH), 7.15 (s, 1H, ArH), 3.91 (s, 6H, OCH_3). FT-IR (ύ max, cm^{-1}): 3362 (NH), 3090 (CH aromatic) 2991 (CH aliphatic), 1705 (C═O), 1625 (C═C), Anal. Calcd for $C_{24}H_{20}N_6O_3$: C, 65.45; H, 4.58; N, 19.08; O, 10.90, Found: C, 65.57; H, 4.56; N, 19.17; O, 10.88. **MS**: (Mwt.:440:m/z, 441 [M$^+$, (38.16%)], 440 (43.42%), 98 (100%).

*4.1.4.6. 5-((6,7-Dimethoxyquinazolin-4-yl)amino)-N-phenyl-1H-indazole-1-carbothioamide **(8f)***. The product was separated as white powder. (38 mg, 13.37%) m.p.: 208–211 °C, ^{1}H NMR (300 MHz, DMSO-d_6) δ 11.22 (s, 1H, NH), 9.2 (s, 1H, NH), 8.78 (s, 1H, ArH), 8.13 (s, 1H, ArH), 8.10 (s, 1H, ArH), 7.98 (s, 1H, ArH), 7.66 (d, J = 8.9 Hz, 1H, ArH), 7.53 (d, J = 8.9 Hz, 1H, ArH), 7.47–7.33 (m, 5H, ArH), 7.27 (s, 1H, ArH), 3.99 (s, 6H, OCH_3).

*4.1.5. 6,7-Dimethoxy-4-(5-nitro-1H-indazol-1-yl)quinazoline **(9)***

To a solution of 5-nitroindazole **2** (3 g, 18.39 mmol) in dry DMF (55 mL) cooled to 0 °C, NaH (0.735 g, 18.39 mmol, 60% in mineral oil) was added. The mixture was stirred at r.t. for 2 h, then cooled to 0 °C once more before addition of 4-chloro-6,7-dimethoxyquinazoline (4.13 g, 18.39 mmol). The mixture was stirred for 4 h, then quenched with water and filtered. The resulted residue was crystallized from methanol and washed with ether to yield the product as dark orange powder. (5.4 g, 83.58%), m.p.: 236–239 °C, ^{1}H NMR (300 MHz, DMSO-d_6) δ 9.06 (s, 1H, ArH), 8.96 (s, 1H, ArH), 8.87 (d, J = 2.2 Hz, 1H, ArH), 8.64 (d, J = 9.1 Hz, 1H, ArH), 8.40 (d, J = 9.1 Hz, 1H, ArH), 8.32 (s, 1H, ArH), 7.47 (s, 1H, ArH), 4.02 (s, 3H, OCH_3), 3.92 (s, 3H, OCH_3). FT-IR (ύ max, cm^{-1}): 3111 (CH aromatic), 2835 (CH aliphatic), 1616 (C═C), 1567, 1344 (NO_2), Anal. Calcd for $C_{17}H_{13}N_5O_4$: C, 58.12; H, 3.73; N, 19.93; O, 18.22, Found: C, 58.29; H, 3.71; N, 20.18; O, 18.31

*4.1.6. 1-(6,7-Dimethoxyquinazolin-4-yl)-1H-indazol-5-amine **(10)***

A mixture of compound **9** (5 g, 14.23 mmol) and 10% Pd/C (0.5 g.) in THF (200 mL) was heated to 40 °C under H_2 atmosphere (30 psi) for 12 h, after which the mixture was filtered and the filtrate was evaporated under vacuo to yield the titled compound as yellow solid (3.3 g, 72.16%) to be used *in situ* in the following step. The purity of the compound was monitored using TLC (DCM/Methanol 9:1).

*4.1.7. General procedure for preparation of target compounds **(11a-e)***

Compound **10** (0.3 g, 0.93 mmol) is dissolved into DCM (40 mL), and then the appropriate isocyanate (0.93 mmol) is added to the solution. The mixture is stirred at room temperature for 24 hrs and then the precipitate formed was filtered out and crystallized from mixture of THF and DCM to give the titled products **(11a-e)**.

*4.1.7.1. 1-(1-(6,7-Dimethoxyquinazolin-4-yl)-1H-indazol-5-yl)-3-phenylurea **(11a)***. The product was separated as pale yellow powder, (140 mg, 34%) m.p.: 251–254 °C, ^{1}H NMR (300 MHz, DMSO-d_6) δ 9.09 (s, 1H, NH), 8.98 (s, 1H, ArH), 8.78 (s, 1H, NH), 8.82–8.47 (m, 3H, ArH), 8.24 (s, 1H, ArH), 7.62–7.10 (m, 6H, ArH), 6.99 (s, 1H, ArH), 4.02 (s, 3H, OCH_3), 3.92 (s, 3H, OCH_3).^{13}C NMR (101 MHz, DMSO-d_6) δ 155.77, 154.40, 153.22, 152.30, 151.04, 150.23, 140.16, 139.55, 136.13, 129.26, 126.24, 124.17, 122.33, 121.69, 118.72, 116.51, 112.05, 111.76, 109.05, 107.37, 106.06, 105.53, 56.51, 56.12. Anal. Calcd for $C_{24}H_{20}N_6O_3$: C, 65.45; H, 4.58; N, 19.08; O, 10.90, Found: C, 65.68; H, 4.64; N, 19.32; O, 10.88.

*4.1.7.2. 1-(3-Chloro-4-methylphenyl)-3-(1-(6,7-dimethoxyquinazolin-4-yl)-1H-indazol-5-yl)urea **(11b)***. The product was separated as buff powder, (156 mg, 34.18%) m.p.: 253–258 °C. ^{1}H NMR (300 MHz, DMSO-d_6) δ 8.93 (s, 1H, ArH), 8.91 (s, 1H, NH), 8.78–8.70 (m, 2H, NH, ArH), 8.59–8.44 (m, 2H, ArH), 8.09 (s, 1H, ArH), 7.64 (s, 1H, ArH), 7.49 (d, J = 9.2 Hz, 1H, ArH), 7.35 (d, J = 8.1 Hz, 1H, ArH), 7.22–7.14 (m, 2H, ArH), 3.98 (s, 3H, OCH_3), 3.94 (s, 3H, OCH_3), 2.21 (s, 3H, CH_3). FT-IR (ύ max, cm^{-1}): 3292 (NH), 3137 (CH aromatic), 2927 (CH aliphatic), 1638 (C═O), 1576 (C═C). Anal. Calcd for $C_{25}H_{21}ClN_6O_3$: C, 61.41; H, 4.33; N, 17.19, Found: C, 61.62; H, 4.30; N, 17.37.

*4.1.7.3. 1-(3,4-Dichlorophenyl)-3-(1-(6,7-dimethoxyquinazolin-4-yl)-1H-indazol-5-yl)urea **(11c)***. The product was separated as yellow powder, (200 mg, 42%) m.p.: 233–238 °C. ^{1}H NMR (300 MHz, DMSO-d_6) δ 9.21 (s, 1H, ArH), 9.13–8.79 (m, 3H, 2NH, 1ArH), 8.58 (d, J = 9.2 Hz, 1H, ArH), 8.26–7.81 (m, 2H, ArH), 7.73 (d, J = 10.6 Hz, 1H, ArH), 7.86–7.45 (m, 2H, ArH), 7.35 (s, 2H, ArH), 3.95 (s, 6H, OCH_3). FT-IR (ύ max, cm^{-1}): 3277 (NH), 3021 (CH aromatic), 2928 (CH aliphatic), 1636 (C═O), 1570 (C═C). Anal. Calcd for $C_{24}H_{18}Cl_2N_6O_3$: C, 56.59; H, 3.56; N, 16.50, Found: C, 56.71; H, 3.60; N, 16.71.

*4.1.7.4. 1-(3-Bromophenyl)-3-(1-(6,7-dimethoxyquinazolin-4-yl)-1H-indazol-5-yl)urea **(11d)***. The product was separated as buff powder, (120 mg, 24.75%) m.p.: 222–224 °C, ^{1}H NMR (300 MHz, DMSO-d_6) δ 9.18 (s, 1H, ArH), 8.98 (s, 1H, ArH), 8.89 (s, 2H, NH), 8.62–8.51 (m, 2H, ArH), 8.15 (d, J = 2.1 Hz, 1H, ArH), 8.06–7.97 (m, 1H, ArH), 7.75 (d, J = 9.4 Hz, 1H, ArH), 7.53 (dd, J = 9.1, 2.2 Hz, 1H), 7.33–7.25 (m, 2H, ArH), 7.12 (s, 1H, ArH), 3.96 (s, 3H, OCH_3), 3.93 (s, 3H, OCH_3). FT-IR (ύ max, cm^{-1}): 3285 (NH), 3129 (CH aromatic), 2931 (CH aliphatic), 1638 (C═O), 1600 (C═C). Anal. Calcd for$C_{24}H_{19}BrN_6O_3$: C, 55.50; H, 3.69; N, 16.18, Found: C, 55.67; H, 3.73; N, 16.34.

*4.1.7.5. 1-(5-Chloro-2,4-dimethoxyphenyl)-3-(1-(6,7-dimethoxyquinazolin-4-yl)-1H-indazol-5-yl)urea **(11e)***. The product was separated as bright yellow powder, (216 mg, 44.5%) m.p.: 268–270 °C, ^{1}H NMR (300 MHz, DMSO-d_6) δ 9.56 (s, 1H, NH), 9.01 (s, 1H, ArH), 8.65 (s, 1H, ArH), 8.61 (s, 1H, ArH), 8.57 (d, J = 9.2 Hz, 1H, ArH), 8.23 (d, 2H, ArH, NH), 8.19 (d, J = 1.4 Hz, 1H, ArH), 7.49 (d, J = 9.4 Hz, 1H, ArH), 7.42 (s, 1H, ArH), 6.87 (s, 1H, ArH), 4.02 (s, 3H, OCH_3), 3.96–3.92 (m, 6H, OCH_3), 3.87 (s, 3H, OCH_3).^{13}C NMR (101 MHz, DMSO-d_6) δ 154.36, 153.08, 152.27, 151.79, 151.01, 149.98, 148.16, 139.52, 136.21, 126.24, 124.82, 122.87, 121.30, 119.87, 116.57, 111.91, 108.61, 107.33, 105.57, 98.48, 56.90, 56.47, 56.08. Anal. Calcd for $C_{26}H_{23}ClN_6O_5$: C, 58.38; H, 4.33; N, 15.71, Found: C, 58.54; H, 4.38; N, 15.79.

4.2. In vitro VEGFR-2 tyrosine kinase activity.

Evaluation of the *in vitro* VEGFR-2 kinase activity was carried out in BPS Bioscience Corporation, San Diego, CA, USA (www.bpsbioscience.com). The assay was performed using Kinase-Glo Plus luminescence kinase assay kit (Promega). It measures kinase activity by quantitating the amount of ATP remaining in solution following a kinase reaction. The luminescent signal from the assay is correlated with the amount of ATP present and is inversely correlated with the amount of kinase activity. The compounds were diluted in 10% DMSO and 5 µl of the dilution was added to a 50 µl reaction so that the final concentration of DMSO is 1% in all of reactions. All of the enzymatic reactions were conducted at 30 °C for 40 min. The 50 µl reaction mixture contains 40 mM Tris, pH 7.4, 10 mM $MgCl_2$, 0.1 mg/ml BSA, 1 mM DTT, 10 µM ATP, Kinase substrate and the enzyme.

After the enzymatic reaction, 50 µl of Kinase-Glo Plus Luminescence kinase assay solution (Promega) was added to each reaction and incubate the plate for 5 min at room temperature. Luminescence signal was measured using a BioTek *Synergy 2* microplate reader.

Kinase activity assays were performed in duplicate at each concentration. The luminescence data were analyzed using the computer software, Graphpad Prism. The difference between luminescence intensities in the absence of Kinase (Lu_t) and in the presence of Kinase (Lu_c) was defined as 100% activity ($Lu_t - Lu_c$). Using luminescence signal (Lu) in the presence of the compound, % activity was calculated as:

% activity = $[(Lu_t - Lu)/(Lu_t - Lu_c)] \times 100\%$, where Lu = the luminescence intensity in the presence of the compound (all percent activities below zero were shown zero in the table).

The values of % activity versus a series of compound concentrations were then plotted using non-linear regression analysis of Sigmoidal dose-response curve generated with the equation $Y = B + (T - B)/1 + 10^{((LogEC50-X) \times Hill\ Slope)}$, where Y = percent activity, B = minimum percent activity, T = maximum percent activity, X = logarithm of compound and Hill Slope = slope factor or Hill coefficient. The IC_{50} value was determined by the concentration causing a half-maximal percent activity.

The compounds were evaluated at the concentrations of: 1 nM, 50 nM, 100 nM, 1 µM, and 10 µM.

Concentration gap between 1 nM and 50 nM might be too big to precisely measure the IC_{50} lower than 10 nM. Therefore, IC_{50} values of compounds **11b**, **c** and **e** were reassessed using concentrations of: 0.01 nM, 0.1 nM, 1 nM, 10 nM, and 100 nM. The results shown for these compounds are the output of the second performed assay.

4.3. In vitro HUVEC Anti-proliferative assay

This assay was also carried out in BPS Bioscience Corporation, San Diego, CA, USA (www.bpsbioscience.com). HUVEC cells were cultured in Medium 200 with 2% large vessel endothelial supplement (LVES) and 1% Pen-strep. To perform the proliferation assay, HUVEC cells were seeded at 5000 cells/50 µl/well in a 96-well black clear-bottom tissue culture plate. Cells were incubated at 37 °C and 5% CO_2 overnight to allow them to recover and reattach. All the experiments were done with 0.1% DMSO in the growth medium.

Next day cells were treated with test compounds for 72 h. After treatment, cell proliferation was measured by Fluorescent quantitation of alamarBlue reagent. The alamarBlue assay incorporates a fluorometric/colorimetric growth indicator based on detection of metabolic activity. Specifically, resazurin, the active ingredient in the alamarBlue reagent, is blue in color and virtually non-fluorescent. Upon entering cells, resazurin is reduced to resorufin, a compound that is red in color and highly fluorescent. Continued cell growth maintains a reduced environment, therefore increasing the overall fluorescence and color of the media surrounding cells. Our experiment has shown that the fluorescence intensity of alamarBlue reagent was directly proportional to cell number. To perform the alamarBlue assay, 10 µl of alamarBlue reagent was added to each well and the plate was incubated at 37 °C for an additional 2 h.

Fluorescence intensity was measured at an excitation of 530 nm and an emission of 590 nm using a BioTek SynergyTM 2 microplate reader. The reading of the background was reported.

Fluorescent intensity data were analyzed using the computer software, Graphpad Prism. In the absence of the compound, the fluorescent intensity (Ft) in each data set was defined as 100%. In the absence of cells, the fluorescent intensity (Fb) in each data set was defined as 0%. The percent cell in the presence of each compound was calculated according to the following equation: %cell = (F − Fb)/(Ft − Fb), where F = the fluorescent intensity in the presence of the compound, Fb = the fluorescent intensity in the absence of cells, and Ft = the fluorescent intensity in the absence of the compound.

The values of % cell versus a series of compound concentrations were then plotted using non-linear regression analysis of Sigmoidal dose-response curve generated with the equation $Y = B + (T - B)/1 + 10_{50}^{((LogEC-X) \times Hill\ Slope)}$, where Y = percent cell, B = minimum percent cell, T = maximum percent cell, X = logarithm of compound and

Hill Slope = slope factor or Hill coefficient. The reported values represent the average of the three experiments. The IC_{50} value was determined by the concentration causing a half-maximal percent activity.

4.4. In vitro HUVEC IC_{50} determination:

The determination of IC_{50} of **11c** against HUVEC cell line was carried out at Vacsera-Egypt, where the HUVEC umbilical vein endothelial cells, human (Life Technologies#C-003-5C) served as the cells' source, in Medium 200 (Life Technologies#M-200-500), with large vessel endothelial supplement (LVES) (Life Technologies#A14608-01) and Penstep (Hyclone#SV30010). Alamar Blue (Life Technologies#DAL1025) was used as the fluorescent reagent (see supplementary file).

4.5. In vitro Anti-proliferative activity against NCI-60 panel

The *in vitro* anticancer activity of the newly synthesized compounds was evaluated by the National Cancer Institute anticancer screening program (National Cancer Institute Bethesda, Maryland, USA). The human tumour cell lines of the cancer-screening panel are grown in RPMI-1640 medium. This medium contains 5% fetal bovine serum and 2 mM L-glutamine. To achieve typical screening experiment, cells were inoculated into 96 well microtiter plates in 100 pL. The plating densities ranged from 5000 to 40,000 cells/well. This depended on the doubling time of individual cell lines. After the cell inoculation, incubation of the microtiter plates at 37 °C, 5% CO_2, 95% air and 100% relative humidity for 24 h was done, before adding the experimental drugs.

After twenty four hours, two plates of each cell line are fixed *in situ* with TCA, to get a measurement of the cell population at the time of tested compound addition for each cell line (Tz). Experimental drugs are dissolved in DMSO at 400-fold the required final maximum test concentration and stored frozen, before being used. At the time of drug addition, an aliquot of the frozen concentrate is melted and diluted to twice the desired final maximum test concentration, where the complete medium contained 50 mg/ml gentamicin.

In addition, 10-fold orlog serial dilutions were prepared to provide a total of five drug concentrations plus control. Aliquots of 100 mL of these drug dilutions were added to the appropriate microtiter wells that contained 100 mL of medium, to give the required final drug concentrations. After adding the drug, the plates are incubated for an extra 48 h at 37 °C, 5% CO_2, 95% air, and 100% relative humidity. As for the adherent cells, the assay was terminated by the adding the cold TCA. Cells were fixed *in situ* by the gentle addition of 50 mL of cold 50% (w/v) TCA (final concentration, 10% TCA) and incubated at 4 °C for 60 min. The supernatant was discarded, and the plates were washed five times, using tap water, then, it was air dried. Sulforhodamine B (SRB) solution (100 mL) at 0.4% (w/v) in 1% acetic acid was added to each well, and the plates were incubated at room temperature for 10 min.

After staining, the unbound dye was removed by washing five times with 1% acetic acid and then, the plates were air dried. Bound stain was subsequently dissolved with 10 mM trizma base, and the absorbance was read on an automated plate reader, using a wavelength of 515 nm. For the suspension cells, the methodology applied was the same, but the assay was terminated through fixing the settled cells at the bottom of the wells by slowly adding 50 mL of 80% TCA, where the final concentration was 16% TCA). Seven absorbance measurements were recorded: [time zero, (Tz), control growth, (C), and test growth in the presence of drug at the five concentration levels (Ti)], the percentage growth is calculated at each of the drug concentrations levels. Percentage growth inhibition was calculated as:

$[(Ti - Tz)/(C - Tz)] \times 100$ for concentrations for which $Ti \geq Tz$
$[(Ti - Tz)/Tz] \times 100$ for concentrations for which $Ti < Tz$.

For each experimental agent, three dose response parameters were calculated. Growth inhibition by 50% (GI_{50}) was calculated by $[(Ti - Tz)/(C - Tz)j \times 100 = 50$, it is the drug concentration that makes a 50% reduction in the net protein increase (as measured by SRB staining) in control cells during the drug incubation. Concentration of the drug that leads to total growth inhibition (TGI) was calculated by $Ti = Tz$. The LC_{50} is the drug concentration that causes a 50% reduction in the measured protein at the end of the drug treatment as compared to that at the beginning. It indicates the net loss of cells after the treatment. It was calculated using the formula: $[(Ti - Tz)/Tzj \times 100 = -50$. Values were calculated for each of these three parameters, if the level of activity is reached. Nevertheless, when the effect was not reached or was exceeded, the value for that parameter was expressed as greater or less than the maximum or minimum concentration tested.

4.6. Effect on Akt and ERK phsophorylation/activation

The effect of PT on AKT activation in PC-3 cells was assessed using phospho-AKT 1/2/3 (Ser473) and phospho-ERK1/2 InstantOne™ ELISA kit (eBiosciences, San Diego, CA). These kits were developed to detect phosphorylation at AKT1/2/3(Ser473) and ERK1/2(Thr202/Tyr204, Thr185/Tyr187) respectively. PC-3 cells were seeded into 96- well plates at a density of 3×10^4 cells/well and incubated overnight to allow for attachment. The tested compounds were added at concentrations equal to the IC50. After 48 h of exposure, the medium was discarded and the wells were washed twice with Hank's buffered salt solution. Akt and ERK activity was determined in the cell lysates as previously described by Tolba and Abdel-Rahman [116].

4.7. Effect on caspase-3 activity

Caspase-3 activity was evaluated using colorimetric protease assay kit (R&D Systems, Minneapolis, MN). At the end of exposures, about 2×10^6 cells were collected and the pellet was resuspended in lysis buffer. Protein levels were determined using BCA protein assay (BioVision, Inc., Milpitas, CA, USA). Aliquots of 50 µl of cell lysate (total protein, 100 µg) were incubated with 5 µl of caspase-3 colorimetric substrate (DEVD-pNA) at 37 °C for 2 h. The activity was expressed as optical density of the released pNA measured at 405 nm using microplate reader (ChroMate-4300, Palm City, FL).

4.8. Statistical analysis

Data of caspase-3 activity, Akt and ERK phsophorylation/activation, are presented as means ± SD. Individual groups were compared using the two-tailed independent Student's *t*-test. Multiple group comparisons were carried out using one-way analysis of variance (ANOVA) followed by the Tukey-Kramer test for post-hoc analysis. Statistical significance was accepted at a level of $P < 0.05$. All statistical analyses were performed using GraphPadInStat software, version 3.05 (GraphPad Software, Inc. La Jolla, CA, USA). Graphs were sketched using GraphPad Prism software, version 5.00 (GraphPad Software, Inc. La Jolla, CA, USA).

Acknowlegments

The authors are grateful to the Center of Excellence for Drug Discovery and Development Research (Funded by the STDF, project no. **5251**) at the Faculty of Pharmacy, Ain Shams University, for performing the NMR spectroscopy of the compounds. Also, we are grateful to NCI, Maryland USA for carrying out cytotoxicity study.

Appendix A. Supplementary material

Supplementary data to this article can be found online at https://doi.org/10.1016/j.bioorg.2018.10.071.

References

[1] A. Bottos, A. Bardelli, Oncogenes and angiogenesis: a way to personalize anti-angiogenic therapy? Cell. Mol. Life Sci. 70 (2013) 4131–4140.
[2] D. Ribatti, Judah Folkman, a pioneer in the study of angiogenesis, Angiogenesis 11 (2008) 3–10.
[3] N. Nishida, H. Yano, T. Nishida, T. Kamura, M. Kojiro, Angiogenesis in Cancer, Vascular Health and Risk Management 2 (2006) 213–219.
[4] J. Folkman, Tumor angiogenesis: therapeutic implications, N. Engl. J. Med. 285 (1971) 1182–1186.
[5] J. Folkman, Angiogenesis in cancer, vascular, rheumatoid and other disease, Nat. Med. 1 (1995) 27–31.
[6] F. Tomao, A. Papa, L. Rossi, E. Zaccarelli, D. Caruso, F. Zoratto, P. Benedetti Panici, S. Tomao, Angiogenesis and antiangiogenic agents in cervical cancer, Onco Targets Ther. 7 (2014) 2237–2248.
[7] F. Musumeci, M. Radi, C. Brullo, S. Schenone, Vascular endothelial growth factor (VEGF) receptors: drugs and new inhibitors, J. Med. Chem. 55 (2012) 10797–10822.
[8] P.W. Manley, G. Bold, J. Bruggen, G. Fendrich, P. Furet, J. Mestan, C. Schnell, B. Stolz, T. Meyer, B. Meyhack, W. Stark, A. Strauss, J. Wood, Advances in the structural biology, design and clinical development of VEGF-R kinase inhibitors for the treatment of angiogenesis, Biochim. Biophys. Acta 1697 (2004) 17–27.
[9] K. Holmes, O.L. Roberts, A.M. Thomas, M.J. Cross, Vascular endothelial growth factor receptor-2: structure, function, intracellular signalling and therapeutic inhibition, Cell Signal 19 (2007) 2003–2012.
[10] D.J. Kerr, Targeting angiogenesis in cancer: clinical development of bevacizumab, Nat. Clin. Pract. Oncol. 1 (2004) 39–43.
[11] S.J. Boyer, Small molecule inhibitors of KDR (VEGFR-2) kinase: an overview of structure activity relationships, Curr. Top Med. Chem. 2 (2002) 973–1000.
[12] S. Wilhelm, C. Carter, M. Lynch, T. Lowinger, J. Dumas, R.A. Smith, B. Schwartz, R. Simantov, S. Kelley, Discovery and development of sorafenib: a multikinase inhibitor for treating cancer, Nat. Rev. Drug Discovery 5 (2006) 835.
[13] R. Roskoski Jr., Sunitinib: a VEGF and PDGF receptor protein kinase and angiogenesis inhibitor, Biochem. Biophys. Res. Commun. 356 (2007) 323–328.
[14] P.A. Harris, A. Boloor, M. Cheung, R. Kumar, R.M. Crosby, R.G. Davis-Ward, A.H. Epperly, K.W. Hinkle, R.N. Hunter 3rd, J.H. Johnson, V.B. Knick, C.P. Laudeman, D.K. Luttrell, R.A. Mook, R.T. Nolte, S.K. Rudolph, J.R. Szewczyk, A.T. Truesdale, J.M. Veal, L. Wang, J.A. Stafford, Discovery of 5-[[4-[(2,3-dimethyl-2H-indazol-6-yl)methylamino]-2-pyrimidinyl]amino]-2-methyl-b enzenesulfonamide (Pazopanib), a novel and potent vascular endothelial growth factor receptor inhibitor, J. Med. Chem. 51 (2008) 4632–4640.
[15] F.M. Yakes, J. Chen, J. Tan, K. Yamaguchi, Y. Shi, P. Yu, F. Qian, F. Chu, F. Bentzien, B. Cancilla, J. Orf, A. You, A.D. Laird, S. Engst, L. Lee, J. Lesch, Y.C. Chou, A.H. Joly, Cabozantinib (XL184), a novel MET and VEGFR2 inhibitor, simultaneously suppresses metastasis, angiogenesis, and tumor growth, Mol. Cancer Ther. 10 (2011) 2298–2308.
[16] J. Matsui, Y. Funahashi, T. Uenaka, T. Watanabe, A. Tsuruoka, M. Asada, Multi-kinase inhibitor E7080 suppresses lymph node and lung metastases of human mammary breast tumor MDA-MB-231 via inhibition of vascular endothelial growth factor-receptor (VEGF-R) 2 and VEGF-R3 kinase, Clin. Cancer Res. 14 (2008) 5459–5465.
[17] M. Gou, H. Si, Y. Zhang, N. Qian, Z. Wang, W. Shi, G. Dai, Efficacy and safety of apatinib in patients with previously treated metastatic colorectal cancer: a real-world retrospective study, Sci. Rep. 8 (2018) 4602.
[18] N. Imai, M. Shikami, H. Miwa, K. Suganuma, A. Hiramatsu, M. Watarai, A. Satoh, M. Itoh, A. Imamura, H. Mihara, M. Nitta, t(8;21) acute myeloid leukaemia cells are dependent on vascular endothelial growth factor (VEGF)/VEGF receptor type2 pathway and phosphorylation of Akt, Br. J. Haematol. 135 (2006) 673–682.
[19] T.T. Zhao, D. Trinh, C.L. Addison, J. Dimitroulakos, Lovastatin inhibits VEGFR and AKT activation: synergistic cytotoxicity in combination with VEGFR inhibitors, PLoS One 5 (2010) e12563.
[20] A. Ahluwalia, M.K. Jones, S. Szabo, A.S. Tarnawski, Aberrant, ectopic expression of VEGF and VEGF receptors 1 and 2 in malignant colonic epithelial cells. Implications for these cells growth via an autocrine mechanism, Biochem. Biophys. Res. Commun. 437 (2013) 515–520.
[21] Y. Chen, L. Jiang, F. She, N. Tang, X. Wang, X. Li, S. Han, J. Zhu, Vascular endothelial growth factor-C promotes the growth and invasion of gallbladder cancer via an autocrine mechanism, Mol. Cell Biochem. 345 (2010) 77–89.
[22] B. Bonnesen, H. Pappot, J. Holmstav, B.G. Skov, Vascular endothelial growth factor A and vascular endothelial growth factor receptor 2 expression in non-small cell lung cancer patients: relation to prognosis, Lung Cancer 66 (2009) 314–318.
[23] A.M. Devery, R. Wadekar, S.M. Bokobza, A.M. Weber, Y. Jiang, A.J. Ryan, Vascular endothelial growth factor directly stimulates tumour cell proliferation in non-small cell lung cancer, Int. J. Oncol. 47 (2015) 849–856.
[24] S.B. Wedam, J.A. Low, S.X. Yang, C.K. Chow, P. Choyke, D. Danforth, S.M. Hewitt, A. Berman, S.M. Steinberg, D.J. Liewehr, J. Plehn, A. Doshi, D. Thomasson, N. McCarthy, H. Koeppen, M. Sherman, J. Zujewski, K. Camphausen, H. Chen, S.M. Swain, Antiangiogenic and antitumor effects of bevacizumab in patients with inflammatory and locally advanced breast cancer, J. Clin. Oncol. 24 (2006) 769–777.
[25] A. Abdollahi, K.E. Lipson, A. Sckell, H. Zieher, F. Klenke, D. Poerschke, A. Roth, X. Han, M. Krix, M. Bischof, P. Hahnfeldt, H.J. Grone, J. Debus, L. Hlatky, P.E. Huber, Combined therapy with direct and indirect angiogenesis inhibition results in enhanced antiangiogenic and antitumor effects, Cancer Res. 63 (2003) 8890–8898.
[26] K.R. Molhoek, G. Erdag, J.K. Rasamny, C. Murphy, D. Deacon, J.W. Patterson, C.L. Slingluff Jr., D.L. Brautigan, VEGFR-2 expression in human melanoma: revised assessment, Int. J. Cancer 129 (2011) 2807–2815.
[27] U. Adamcic, K. Skowronski, C. Peters, J. Morrison, B.L. Coomber, The effect of bevacizumab on human malignant melanoma cells with functional VEGF/VEGFR2 autocrine and intracrine signaling loops, Neoplasia 14 (2012) 612–623.
[28] Y. Liu, R.T. Poon, Q. Li, T.W. Kok, C. Lau, S.T. Fan, Both antiangiogenesis- and angiogenesis-independent effects are responsible for hepatocellular carcinoma growth arrest by tyrosine kinase inhibitor PTK787/ZK222584, Cancer Res. 65 (2005) 3691–3699.
[29] H.L. Goel, A.M. Mercurio, VEGF targets the tumour cell, nature reviews, Cancer 13 (2013) 871–882.
[30] J. Paesler, I. Gehrke, S.J. Poll-Wolbeck, K.A. Kreuzer, Targeting the vascular endothelial growth factor in hematologic malignancies, Eur. J. Haematol. 89 (2012) 373–384.
[31] G.C. Jayson, R. Kerbel, L.M. Ellis, A.L. Harris, Antiangiogenic therapy in oncology: current status and future directions, Lancet 388 (2016) 518–529.
[32] S.S. Taylor, A.P. Kornev, Protein kinases: evolution of dynamic regulatory proteins, Trends Biochem. Sci. 36 (2011) 65–77.
[33] M. McTigue, B.W. Murray, J.H. Chen, Y.L. Deng, J. Solowiej, R.S. Kania, Molecular conformations, interactions, and properties associated with drug efficiency and clinical performance among VEGFR TK inhibitors, Proc. Natl. Acad. Sci. USA 109 (2012) 18281–18289.
[34] J. Dietrich, C. Hulme, L.H. Hurley, The design, synthesis, and evaluation of 8 hybrid DFG-out allosteric kinase inhibitors: a structural analysis of the binding interactions of Gleevec, Nexavar, and BIRB-796, Bioorg. Med. Chem. 18 (2010) 5738–5748.
[35] L.K. Shawver, D. Slamon, A. Ullrich, Smart drugs: tyrosine kinase inhibitors in cancer therapy, Cancer Cell 1 (2002) 117–123.
[36] Z. Zhao, H. Wu, L. Wang, Y. Liu, S. Knapp, Q. Liu, N.S. Gray, Exploration of type II binding mode: a privileged approach for kinase inhibitor focused drug discovery? ACS Chem. Biol. 9 (2014) 1230–1241.
[37] J.F. Ohren, H. Chen, A. Pavlovsky, C. Whitehead, E. Zhang, P. Kuffa, C. Yan, P. McConnell, C. Spessard, C. Banotai, W.T. Mueller, A. Delaney, C. Omer, J. Sebolt-Leopold, D.T. Dudley, I.K. Leung, C. Flamme, J. Warmus, M. Kaufman, S. Barrett, H. Tecle, C.A. Hasemann, Structures of human MAP kinase kinase 1 (MEK1) and MEK2 describe novel noncompetitive kinase inhibition, Nat. Struct. Mol. Biol. 11 (2004) 1192–1197.
[38] L. Tatton, G.M. Morley, R. Chopra, A. Khwaja, The Src-selective kinase inhibitor PP1 also inhibits Kit and Bcr-Abl tyrosine kinases, J. Biol. Chem. 278 (2003) 4847–4853.
[39] H. Iwata, H. Oki, K. Okada, T. Takagi, M. Tawada, Y. Miyazaki, S. Imamura, A. Hori, J.D. Lawson, M.S. Hixon, H. Kimura, H. Miki, A back-to-front fragment-based drug design search strategy targeting the DFG-out pocket of protein tyrosine kinases, ACS Med. Chem. Lett. 3 (2012) 342–346.
[40] M.A. Abdullaziz, H.T. Abdel-Mohsen, A.M. El Kerdawy, F.A.F. Ragab, M.M. Ali, S.M. Abu-Bakr, A.S. Girgis, H.I. El Diwani, Design, synthesis, molecular docking and cytotoxic evaluation of novel 2-furybenzimidazoles as VEGFR-2 inhibitors, Eur. J. Med. Chem. 136 (2017) 315–329.
[41] R.S.K. Vijayan, P. He, V. Modi, K.C. Duong-Ly, H. Ma, J.R. Peterson, R.L. Dunbrack, R.M. Levy, Conformational analysis of the DFG-out Kinase motif and biochemical profiling of structurally validated Type II inhibitors, J. Med. Chem. 58 (2015) 466–479.
[42] K. Lee, K.W. Jeong, Y. Lee, J.Y. Song, M.S. Kim, G.S. Lee, Y. Kim, Pharmacophore modeling and virtual screening studies for new VEGFR-2 kinase inhibitors, Eur. J. Med. Chem. 45 (2010) 5420–5427.
[43] Y. Dai, K. Hartandi, Z. Ji, A.A. Ahmed, D.H. Albert, J.L. Bauch, J.J. Bouska, P.F. Bousquet, G.A. Cunha, K.B. Glaser, C.M. Harris, D. Hickman, J. Guo, J. Li, P.A. Marcotte, K.C. Marsh, M.D. Moskey, R.L. Martin, A.M. Olson, D.J. Osterling, L.J. Pease, N.B. Soni, K.D. Stewart, V.S. Stoll, P. Tapang, D.R. Reuter, S.K. Davidsen, M.R. Michaelides, Discovery of N-(4-(3-amino-1H-indazol-4-yl) phenyl)-N'-(2-fluoro-5-methylphenyl)urea (ABT-869), a 3-aminoindazole-based orally active multitargeted receptor tyrosine kinase inhibitor, J. Med. Chem. 50 (2007) 1584–1597.
[44] A. Wissner, H.L. Fraser, C.L. Ingalls, R.G. Dushin, M.B. Floyd, K. Cheung, T. Nittoli, M.R. Ravi, X. Tan, F. Loganzo, Dual irreversible kinase inhibitors: Quinazoline-based inhibitors incorporating two independent reactive centers with each targeting different cysteine residues in the kinase domains of EGFR and VEGFR-2, Bioorg. Med. Chem. 15 (2007) 3635–3648.
[45] W. Zhan, L. Xu, X. Dong, J. Dong, X. Yi, X. Ma, N. Qiu, J. Li, B. Yang, Y. Zhou, Y. Hu, Design, synthesis and biological evaluation of pyrazol-furan carboxamide analogues as novel Akt kinase inhibitors, Eur. J. Med. Chem. 117 (2016) 47–58.
[46] Z. Fang, Y. Song, P. Zhan, Q. Zhang, X. Liu, Conformational restriction: an effective tactic in 'follow-on'-based drug discovery, Future Med. Chem. 6 (2014) 885–901.
[47] N.M.Y. Elsayed, D.A.A.E. Ella, R.A.T. Serya, M.F. Tolba, R. Shalaby, K.A.M. Abouzid, Design, synthesis and biological evaluation of indazole–pyrimidine based derivatives as anticancer agents with anti-angiogenic and antiproliferative activities, MedChemComm 7 (2016) 881–899.
[48] D.S. La, J. Belzile, J.V. Bready, A. Coxon, T. DeMelfi, N. Doerr, J. Estrada, J.C. Flynn, S.R. Flynn, R.F. Graceffa, S.P. Harriman, J.F. Larrow, A.M. Long, M.W. Martin, M.J. Morrison, V.F. Patel, P.M. Roveto, L. Wang, M.M. Weiss, D.A. Whittington, Y. Teffera, Z. Zhao, A.J. Polverino, J.C. Harmange, Novel 2,3-dihydro-1,4-benzoxazines as potent and orally bioavailable inhibitors of tumor-driven angiogenesis, J. Med. Chem. 51 (2008) 1695–1705.
[49] E.L. Meredith, N. Mainolfi, S. Poor, Y. Qiu, K. Miranda, J. Powers, D. Liu, F. Ma,

C. Solovay, C. Rao, L. Johnson, N. Ji, G. Artman, L. Hardegger, S. Hanks, S. Shen, A. Woolfenden, E. Fassbender, J.M. Sivak, Y. Zhang, D. Long, R. Cepeda, F. Liu, V.P. Hosagrahara, W. Lee, P. Tarsa, K. Anderson, J. Elliott, B. Jaffee, Discovery of Oral VEGFR-2 inhibitors with prolonged ocular retention that are efficacious in models of wet age-related macular degeneration, J. Med. Chem. 58 (2015) 9273–9286.
[50] G. Bold, C. Schnell, P. Furet, P. McSheehy, J. Bruggen, J. Mestan, P.W. Manley, P. Druckes, M. Burglin, U. Durler, J. Loretan, R. Reuter, M. Wartmann, A. Theuer, B. Bauer-Probst, G. Martiny-Baron, P. Allegrini, A. Goepfert, J. Wood, A. Littlewood-Evans, A novel potent oral series of VEGFR2 inhibitors abrogate tumor growth by inhibiting angiogenesis, J. Med. Chem. 59 (2016) 132–146.
[51] Y. Lv, M. Li, T. Liu, L. Tong, T. Peng, L. Wei, J. Ding, H. Xie, W. Duan, Discovery of a new series of naphthamides as potent VEGFR-2 kinase inhibitors, ACS Med. Chem. Lett. 5 (2014) 592–597.
[52] Y. Lv, M. Li, S. Cao, L. Tong, T. Peng, L. Wei, H. Xie, J. Ding, W. Duan, Discovery of anilinopyrimidine-based naphthamide derivatives as potent VEGFR-2 inhibitors, MedChemComm 6 (2015) 1375–1380.
[53] J.C. Harmange, M.M. Weiss, J. Germain, A.J. Polverino, G. Borg, J. Bready, D. Chen, D. Choquette, A. Coxon, T. DeMelfi, L. DiPietro, N. Doerr, J. Estrada, J. Flynn, R.F. Graceffa, S.P. Harriman, S. Kaufman, D.S. La, A. Long, M.W. Martin, S. Neervannan, V.F. Patel, M. Potashman, K. Regal, P.M. Roveto, M.L. Schrag, C. Starnes, A. Tasker, Y. Teffera, L. Wang, R.D. White, D.A. Whittington, R. Zanon, Naphthamides as novel and potent vascular endothelial growth factor receptor tyrosine kinase inhibitors: design, synthesis, and evaluation, J. Med. Chem. 51 (2008) 1649–1667.
[54] N. Mainolfi, J. Powers, E. Meredith, J. Elliott, K.G. Gunderson, S. Poor, F. Liu, K. Anderson, Core replacements in a potent series of VEGFR-2 inhibitors and their impact on potency, solubility, and hERG, ACS Med. Chem. Lett. 7 (2016) 357–362.
[55] X. Zhang, S. Raghavan, M. Ihnat, E. Hamel, C. Zammiello, A. Bastian, S.L. Mooberry, A. Gangjee, The design, synthesis and biological evaluation of conformationally restricted 4-substituted-2,6-dimethylfuro[2,3-d]pyrimidines as multi-targeted receptor tyrosine kinase and microtubule inhibitors as potential antitumor agents, Bioorg. Med. Chem. 23 (2015) 2408–2423.
[56] T.J. Ritchie, S.J.F. Macdonald, S. Peace, S.D. Pickett, C.N. Luscombe, The developability of heteroaromatic and heteroaliphatic rings – do some have a better pedigree as potential drug molecules than others? MedChemComm 3 (2012) 1062–1069.
[57] I. Denya, S.F. Malan, J. Joubert, Indazole derivatives and their therapeutic applications: a patent review (2013–2017), Expert Opin. Ther. Pat. 28 (2018) 441–453.
[58] A. Garofalo, L. Goossens, P. Six, A. Lemoine, S. Ravez, A. Farce, P. Depreux, Impact of aryloxy-linked quinazolines: a novel series of selective VEGFR-2 receptor tyrosine kinase inhibitors, Bioorg. Med. Chem. Lett. 21 (2011) 2106–2112.
[59] P.A. Plé, F. Jung, S. Ashton, L. Hennequin, R. Laine, R. Morgentin, G. Pasquet, S. Taylor, Discovery of AZD2932, a new quinazoline ether inhibitor with high affinity for VEGFR-2 and PDGFR tyrosine kinases, Bioorg. Med. Chem. Lett. 22 (2012) 262–266.
[60] L. Shi, T.-T. Wu, Z. Wang, J.-Y. Xue, Y.-G. Xu, Discovery of quinazolin-4-amines bearing benzimidazole fragments as dual inhibitors of c-Met and VEGFR-2, Bioorg. Med. Chem. 22 (2014) 4735–4744.
[61] A. Garofalo, A. Farce, S. Ravez, A. Lemoine, P. Six, P. Chavatte, L. Goossens, P. Depreux, Synthesis and structure-activity relationships of (aryloxy)quinazoline ureas as novel, potent, and selective vascular endothelial growth factor receptor-2 inhibitors, J. Med. Chem. 55 (2012) 1189–1204.
[62] F. Ciardiello, R. Bianco, R. Caputo, R. Caputo, V. Damiano, T. Troiani, D. Melisi, F. De Vita, S. De Placido, A.R. Bianco, G. Tortora, Antitumor activity of ZD6474, a vascular endothelial growth factor receptor tyrosine kinase inhibitor, in human cancer cells with acquired resistance to antiepidermal growth factor receptor therapy, Clin. Cancer Res. 10 (2004) 784–793.
[63] H.-Q. Zhang, F.-H. Gong, J.-Q. Ye, C. Zhang, X.-H. Yue, C.-G. Li, Y.-G. Xu, L.-P. Sun, Design and discovery of 4-anilinoquinazoline-urea derivatives as dual TK inhibitors of EGFR and VEGFR-2, Eur. J. Med. Chem. 125 (2017) 245–254.
[64] J. Sun, D.D. Li, J.R. Li, F. Fang, Q.R. Du, Y. Qian, H.L. Zhu, Design, synthesis, biological evaluation, and molecular modeling study of 4-alkoxyquinazoline derivatives as potential VEGFR2 kinase inhibitors, Org. Biomol. Chem. 11 (2013) 7676–7686.
[65] P. Pathak, P.K. Shukla, V. Kumar, A. Kumar, A. Verma, Quinazoline clubbed 1,3,5-triazine derivatives as VEGFR2 kinase inhibitors: design, synthesis, docking, in vitro cytotoxicity and in ovo antiangiogenic activity, Inflammopharmacology (2018).
[66] D. Goff, J. Zhang, T. Heckrodt, J. Yu, P. Ding, R. Singh, S. Holland, W. Li, M. Irving, Discovery of dual Axl/VEGF-R2 inhibitors as potential anti-angiogenic and anti-metastatic drugs for cancer chemotherapy, Bioorg. Med. Chem. Lett. 27 (2017) 3766–3771.
[67] Y. Zhang, Y. Chen, D. Zhang, L. Wang, T. Lu, Y. Jiao, Discovery of novel potent VEGFR-2 inhibitors exerting significant antiproliferative activity against cancer cell lines, J. Med. Chem. 61 (2018) 140–157.
[68] I. Khan, A. Ibrar, N. Abbas, A. Saeed, Recent advances in the structural library of functionalized quinazoline and quinazolinone scaffolds: synthetic approaches and multifarious applications, Eur. J. Med. Chem. 76 (2014) 193–244.
[69] W.D.P.H.D. Porter, 5-NITROINDAZOLE, Org. Synth. 3 (1955) 660.
[70] M.N. Nakatsu, R.C. Sainson, J.N. Aoto, K.L. Taylor, M. Aitkenhead, S. Perez-del-Pulgar, P.M. Carpenter, C.C. Hughes, Angiogenic sprouting and capillary lumen formation modeled by human umbilical vein endothelial cells (HUVEC) in fibrin gels: the role of fibroblasts and Angiopoietin-1, Microvasc. Res. 66 (2003) 102–112.
[71] H.J. Park, Y. Zhang, S.P. Georgescu, K.L. Johnson, D. Kong, J.B. Galper, Human umbilical vein endothelial cells and human dermal microvascular endothelial cells offer new insights into the relationship between lipid metabolism and angiogenesis, Stem. Cell Rev. 2 (2006) 93–102.
[72] https://dtp.cancer.gov/discovery_development/nci-60/guidelines.htm, in.
[73] M.R.B.K.D. Paull, Some practical considerations and applications of the national cancer institute in vitro anticancer drug discovery screen, Drug Dev. Res. 34 (1995) 91–109.
[74] G. Luo, Z. Tang, K. Lao, X. Li, Q. You, H. Xiang, Structure-activity relationships of 2, 4-disubstituted pyrimidines as dual ERalpha/VEGFR-2 ligands with anti-breast cancer activity, Eur. J. Med. Chem. 150 (2018) 783–795.
[75] R. Singla, K.B. Gupta, S. Upadhyay, M. Dhiman, V. Jaitak, Design, synthesis and biological evaluation of novel indole-benzimidazole hybrids targeting estrogen receptor alpha (ER-alpha), Eur. J. Med. Chem. 146 (2018) 206–219.
[76] M.S. Elsayed, M.E. El-Araby, R.A. Serya, A.H. El-Khatib, M.W. Linscheid, K.A. Abouzid, Structure-based design and synthesis of novel pseudosaccharine derivatives as antiproliferative agents and kinase inhibitors, Eur. J. Med. Chem. 61 (2013) 122–131.
[77] E. Norris-Cervetto, R. Callaghan, F.M. Platt, R.A. Dwek, T.D. Butters, Inhibition of glucosylceramide synthase does not reverse drug resistance in cancer cells, J. Biol. Chem. 279 (2004) 40412–40418.
[78] G.P. Pidgeon, M.P. Barr, J.H. Harmey, D.A. Foley, D.J. Bouchier-Hayes, Vascular endothelial growth factor (VEGF) upregulates BCL-2 and inhibits apoptosis in human and murine mammary adenocarcinoma cells, Br. J. Cancer 85 (2001) 273–278.
[79] D.J. Price, T. Miralem, S. Jiang, R. Steinberg, H. Avraham, Role of vascular endothelial growth factor in the stimulation of cellular invasion and signaling of breast cancer cells, Cell Growth Differ 12 (2001) 129–135.
[80] H. Wang, H. Gao, N. Guo, G. Niu, Y. Ma, D.O. Kiesewetter, X. Chen, Site-specific labeling of scVEGF with fluorine-18 for positron emission tomography imaging, Theranostics 2 (2012) 607–617.
[81] S. Dias, K. Hattori, Z. Zhu, B. Heissig, M. Choy, W. Lane, Y. Wu, A. Chadburn, E. Hyjek, M. Gill, D.J. Hicklin, L. Witte, M.A.S. Moore, S. Rafii, Autocrine stimulation of VEGFR-2 activates human leukemic cell growth and migration, J. Clin. Invest. 106 (2000) 511–521.
[82] J. Chiu, Y.F. Tang, T.J. Yao, A. Wong, H. Wong, R. Leung, P. Chan, T.T. Cheung, A.C. Chan, R. Pang, S.T. Fan, R. Poon, T. Yau, The use of single-agent sorafenib in the treatment of advanced hepatocellular carcinoma patients with underlying Child-Pugh B liver cirrhosis: a retrospective analysis of efficacy, safety, and survival benefits, Cancer 118 (2012) 5293–5301.
[83] D.J. Mulholland, S. Dedhar, H. Wu, C.C. Nelson, PTEN and GSK3beta: key regulators of progression to androgen-independent prostate cancer, Oncogene 25 (2006) 329–337.
[84] M.A. Davies, The role of the PI3K-AKT pathway in melanoma, Cancer J. 18 (2012) 142–147.
[85] A. Carnero, J.M. Paramio, The PTEN/PI3K/AKT pathway in vivo, Cancer Mouse Models, Front. Oncol. 4 (2014) 252.
[86] D. Papadatos-Pastos, R. Rabbie, P. Ross, D. Sarker, The role of the PI3K pathway in colorectal cancer, Crit. Rev. Oncol. Hematol. 94 (2015) 18–30.
[87] B.A. Jull, H.K. Plummer 3rd, H.M. Schuller, Nicotinic receptormediated activation by the tobacco-specific nitrosamine NNK of a Raf-1/MAP kinase pathway, resulting in phosphorylation of c-myc in human small cell lung carcinoma cells and pulmonary neuroendocrine cells, J. Cancer Res. Clin. Oncol. 127 (2001) 707–717.
[88] V. Grossi, A. Peserico, T. Tezil, C. Simone, p38alpha MAPK pathway: a key factor in colorectal cancer therapy and chemoresistance, World J. Gastroenterol. 20 (2014) 9744–9758.
[89] E.K. Kim, E.-J. Choi, Pathological roles of MAPK signaling pathways in human diseases, Biochim. Biophys. Acta (BBA) – Molecular Basis Disease 1802 (2010) 396–405.
[90] P. Liu, H. Cheng, T.M. Roberts, J.J. Zhao, Targeting the phosphoinositide 3-kinase (PI3K) pathway in cancer, nature reviews, Drug Discovery 8 (2009) 627–644.
[91] S. Huang, P.J. Houghton, Targeting mTOR signaling for cancer therapy, Curr. Opin. Pharmacol. 3 (2003) 371–377.
[92] Z. Jiang, Y. Zou, Z. Ge, Q. Zuo, S.Y. Huang, L. Sun, A role of sFlt-1 in oxidative stress and apoptosis in human and mouse pre-eclamptic trophoblasts, Biol. Reprod. 93 (2015) 73.
[93] T.F. Reubold, S. Eschenburg, A molecular view on signal transduction by the apoptosome, Cell. Signall. 24 (2012) 1420–1425.
[94] D.R. Koes, M.P. Baumgartner, C.J. Camacho, Lessons learned in empirical scoring with smina from the CSAR 2011 benchmarking exercise, J. Chem. Inf. Model 53 (2013) (2011) 1893–1904.
[95] O. Trott, A.J. Olson, AutoDock Vina: improving the speed and accuracy of docking with a new scoring function, efficient optimization, and multithreading, J. Comput. Chem. 31 (2010) 455–461.
[96] K. Okamoto, M. Ikemori-Kawada, A. Jestel, K. von Konig, Y. Funahashi, T. Matsushima, A. Tsuruoka, A. Inoue, J. Matsui, Distinct binding mode of multikinase inhibitor lenvatinib revealed by biochemical characterization, ACS Med. Chem. Lett. 6 (2015) 89–94.
[97] G.M. Sastry, M. Adzhigirey, T. Day, R. Annabhimoju, W. Sherman, Protein and ligand preparation: parameters, protocols, and influence on virtual screening enrichments, J. Comput. Aided Mol. Des. 27 (2013) 221–234.
[98] S.A. Salama, M. Kamel, M. Awad, A.H. Nasser, A. Al-Hendy, S. Botting, C. Arrastia, Catecholestrogens induce oxidative stress and malignant transformation in human endometrial glandular cells: protective effect of catechol-O-methyltransferase, Int. J. Cancer 123 (2008) 1246–1254.
[99] B.R. Miller, T.D. McGee, J.M. Swails, N. Homeyer, H. Gohlke, A.E. Roitberg,

MMPBSA.py: an efficient program for end-state free energy calculations, J. Chem. Theory Comput. 8 (2012) 3314–3321.
[100] D.A. Case, T.A. Darden, T.E. Cheatham, C.L. Simmerling, J. Wang, R.E. Duke, R. Luo, R.C. Walker, W. Zhang, K.M. Merz, B. Roberts, S. Hayik, A. Roitberg, G. Seabra, J. Swails, A.W. Goetz, I. Kolossváry, K.F. Wong, F. Paesani, J. Vanicek, R.M. Wolf, J. Liu, X. Wu, S.R. Brozell, T. Steinbrecher, H. Gohlke, Q. Cai, X. Ye, J. Wang, M.J. Hsieh, G. Cui, D.R. Roe, D.H. Mathews, M.G. Seetin, R. Salomon-Ferrer, C. Sagui, V. Babin, T. Luchko, S. Gusarov, A. Kovalenko, P.A. Kollman, AMBER 14, University of California, San Francisco, 2014.
[101] J. Wang, R.M. Wolf, J.W. Caldwell, P.A. Kollman, D.A. Case, Development and testing of a general amber force field, J. Comput. Chem. 25 (2004) 1157–1174.
[102] J. Wang, W. Wang, P.A. Kollman, D.A. Case, Automatic atom type and bond type perception in molecular mechanical calculations, J. Mol. Graph. Model 25 (2006) 247–260.
[103] T. Darden, D. York, L. Pedersen, Particle mesh Ewald: An N.log(N) method for Ewald sums in large systems, J. Chem. Phys. 98 (1993) 10089–10092.
[104] S. Ravez, S. Arsenlis, A. Barczyk, A. Dupont, R. Frédérick, S. Hesse, G. Kirsch, P. Depreux, L. Goossens, Synthesis and biological evaluation of di-aryl urea derivatives as c-Kit inhibitors, Bioorg. Med. Chem. 23 (2015) 7340–7347.
[105] P.A. Plé, F. Jung, S. Ashton, L. Hennequin, R. Laine, C. Lambert-van der Brempt, R. Morgentin, G. Pasquet, S. Taylor, Discovery of new quinoline ether inhibitors with high affinity and selectivity for PDGFR tyrosine kinases, Bioorg. Med. Chem. Lett. 22 (2012) 3050–3055.
[106] K. Kubo, T. Shimizu, S. Ohyama, H. Murooka, A. Iwai, K. Nakamura, K. Hasegawa, Y. Kobayashi, N. Takahashi, K. Takahashi, S. Kato, T. Izawa, T. Isoe, Novel potent orally active selective VEGFR-2 tyrosine kinase inhibitors: synthesis, structure-activity relationships, and antitumor activities of N-phenyl-N'-{4-(4-quinolyloxy) phenyl}ureas, J. Med. Chem. 48 (2005) 1359–1366.
[107] M. Ahmed, M.M. Sadek, K.A. Abouzid, F. Wang, In silico design: extended molecular dynamic simulations of a new series of dually acting inhibitors against EGFR and HER2, J. Mol. Graph. Model 44 (2013) 220–231.
[108] M. Ahmed, M.M. Sadek, R.A. Serrya, A.H. Kafafy, K.A. Abouzid, F. Wang, Assessment of new anti-HER2 ligands using combined docking, QM/MM scoring and MD simulation, J. Mol. Graph. Model 40 (2013) 91–98.
[109] M.M. Sadek, R.A. Serrya, A.H. Kafafy, M. Ahmed, F. Wang, K.A. Abouzid, Discovery of new HER2/EGFR dual kinase inhibitors based on the anilinoquinazoline scaffold as potential anti-cancer agents, J. Enzyme Inhib. Med. Chem. 29 (2014) 215–222.
[110] D. Choquette, Y. Teffera, A. Polverino, J.C. Harmange, Discovery of novel 1,2,3,4-tetrahydroisoquinolines and 3,4-dihydroisoquinoline-1(2H)-ones as potent and selective inhibitors of KDR: synthesis SAR, and pharmacokinetic properties, Bioorg. Med. Chem. Lett. 18 (2008) 4054–4058.
[111] J. Du, B. Lei, J. Qin, H. Liu, X. Yao, Molecular modeling studies of vascular endothelial growth factor receptor tyrosine kinase inhibitors using QSAR and docking, J. Mol. Graph. Model 27 (2009) 642–654.
[112] X.W. Zhao, D. Liu, S.L. Luan, G.D. Hu, J.L. Lv, Y.K. Jing, L.X. Zhao, Synthesis and biological evaluation of substituted 1,2,3-benzotriazines and pyrido[3,2-d]-1,2,3-triazines as inhibitors of vascular endothelial growth factor receptor-2, Bioorg. Med. Chem. 21 (2013) 7807–7815.
[113] X. Lin, X.P. Huang, G. Chen, R. Whaley, S. Peng, Y. Wang, G. Zhang, S.X. Wang, S. Wang, B.L. Roth, N. Huang, Life beyond kinases: structure-based discovery of sorafenib as nanomolar antagonist of 5-HT receptors, J. Med. Chem. 55 (2012) 5749–5759.
[114] M. Chakrabarty, T. Kundu, S. Arima, Y. Harigaya, An expedient, regioselective synthesis of novel 2-alkylamino- and 2-alkylthiothiazolo[5,4-e]- and -[4,5-g]indazoles and their anticancer potential, Tetrahedron 64 (2008) 6711–6723.
[115] W.-G.J. Su, Hong, Zhang Weihan, Cui Yumin, Yan Xiaoqiang, Ren Yongxin, Duan Jifeng, Sai Yang, Preparation of pyrimidine derivatives for treating angiogenesis-related disorders, in: Hutchison MediPharma Enterprises Limeted, Nassau (BS), Shanghai, 2008, pp. 1–74.
[116] M.F. Tolba, S.Z. Abdel-Rahman, Pterostilbine, an active component of blueberries, sensitizes colon cancer cells to 5-fluorouracil cytotoxicity, Sci Rep. 5 (2015) 15239.